

# Hyaluronic acid-functionalized bismuth oxide nanoparticles for computed tomography imaging-guided radiotherapy of tumor

Fengyi Du<sup>1,2,\*</sup>  
Jiaming Lou<sup>1,\*</sup>  
Rong Jiang<sup>2,\*</sup>  
Zhengzhou Fang<sup>2,\*</sup>  
Xuefen Zhao<sup>2</sup>  
Yuanyuan Niu<sup>2</sup>  
Shenqiang Zou<sup>3</sup>  
Miaomiao Zhang<sup>2</sup>  
Aihua Gong<sup>2</sup>  
Chaoyang Wu<sup>1</sup>

<sup>1</sup>Department of Oncology, The Affiliated People's Hospital, Jiangsu University, Zhenjiang, People's Republic of China; <sup>2</sup>Department of Cellular Biology, School of Medicine, Jiangsu University, Zhenjiang, People's Republic of China; <sup>3</sup>Department of Hepatosis, The Third Hospital of Zhenjiang Affiliated, Jiangsu University, Zhenjiang, People's Republic of China

\*These authors contributed equally to this work

Correspondence: Chaoyang Wu  
Department of Oncology, The Affiliated People's Hospital, Jiangsu University, Dianli Road, Zhenjiang 212002, People's Republic of China  
Email wuchaoyang9@163.com

**Abstract:** The inherent radioresistance and inaccuracy of localization of tumors weaken the clinical implementation effectiveness of radiotherapy. To overcome these limitations, hyaluronic acid-functionalized bismuth oxide nanoparticles (HA-Bi<sub>2</sub>O<sub>3</sub> NPs) were synthesized by one-pot hydrothermal method for target-specific computed tomography (CT) imaging and radiosensitization of tumor. After functionalization with hyaluronic acid, the Bi<sub>2</sub>O<sub>3</sub> NPs possessed favorable solubility in water and excellent biocompatibility and were uptaken specifically by cancer cells overexpressing CD44 receptors. The as-prepared HA-Bi<sub>2</sub>O<sub>3</sub> NPs exhibited high X-ray attenuation efficiency and ideal radiosensitivity via synergizing X-rays to induce cell apoptosis and arrest the cell cycle in a dose-dependent manner in vitro. Remarkably, these properties offered excellent performance in active-targeting CT imaging and enhancement of radiosensitivity for inhibition of tumor growth. These findings demonstrated that HA-Bi<sub>2</sub>O<sub>3</sub> NPs as theranostic agents exhibit great promise for CT imaging-guided radiotherapy in diagnosis and treatment of tumors.

**Keywords:** HA-Bi<sub>2</sub>O<sub>3</sub> NPs, CT imaging, radiosensitivity, HA, bismuth

## Introduction

Radiotherapy has been extensively applied in cancer therapy except for surgery and chemotherapy. This technique employs high-energy X-rays and involves deposition of irradiation doses in tumor sites by causing free radical damage or DNA damage.<sup>1-4</sup> However, poor radiosensitivity or inherent radioresistance of tumors leads to utilization of higher irradiation doses for effective elimination of cancer cells; this radioresistance is caused by various mechanisms (eg, hypoxic, S-phase) which may finally limit the clinical implementation of radiotherapy. Besides, inaccuracy of tumor localization and poor discrimination between lesion and tumor-surrounding tissues lead to inadequate dose coverage to the lesion tissues and overexposure to normal tissues,<sup>5</sup> which results in the occurrence of irradiation side effects and failure of tumor control as well as cancer recurrence. Therefore, development of a new effective way for enhancing tumor radiosensitivity while minimizing systemic side effects becomes an urgent strategy. In this aspect, combining chemotherapy and radiotherapy is a well-established technique for radiosensitization. The newly developed theranostic formulations offer several advantages including assessment of biodistribution and noninvasive accumulation of drugs at target sites, visualization of drug distribution and drug release at the target site, optimization of formulation which relies on triggered drug release, and real-time monitoring of the therapeutic responses with the help of different kinds of imaging modalities.<sup>6</sup>

In recent years, nanotechnology has been considered as an attractive strategy for cancer diagnostics and therapy owing to its multifunctional applications in tumor-targeted drug delivery and drug localization.<sup>7-12</sup> Additionally, nanoparticles (NPs) could be ideal candidates for accurate tumor-targeting imaging to locate tumors because of their prolonged circulation time, selective accumulation in tumors by the enhanced permeability and retention effect, and active targeting through conjugating with folic acid, antibodies, peptides, or hyaluronic acid (HA).<sup>13</sup> In addition, the X-ray dose of the surrounding tissue will be greatly reduced, and higher dose can be concentrated at the tumor region containing NPs. Interestingly, NPs were designed to serve as radiosensitization enhancers.<sup>14-16</sup> Heavy metal (with high-Z elements such as Au, Pt, Bi, Ta, Gd, and Lu<sup>17,18</sup>) NPs as promising computed tomography (CT) contrast agents (CAs) could be used in radiosensitizing therapy because of their high X-ray photon capture cross-section and Compton scattering effect. When X-rays interact with high-Z NPs, Auger electrons and photoelectrons are emitted, with diameters ranging from nanometers to several micrometers. Furthermore, when photon beams of kilovolt and megavolt energy interact with high-Z NPs in a tumor, the release of secondary electrons can injure tumor cells, leading to a higher treatment efficacy than radiation alone.

CT is a mainstay of clinical diagnostic modality with the advantages of high resolution, no depth limitation, and possibility of three-dimensional reconstruction. However, pharmacokinetic limitations of clinically available CT CAs (small iodinated molecules), including short circulation half-lives and nonspecific distribution, are the main causes of CT failure for tumor-targeting imaging and angiography. Moreover, various intrinsic limitations of CT imaging particularly with respect to inadequate soft tissue contrast, low-throughput capacity, limited accessibility, and ionizing radiation are also considered as notable hurdles that prevent the application of CT for clinical diagnosis.<sup>19</sup>

To date, bismuth-based NPs (BiNPs) such as Bi<sub>2</sub>S<sub>3</sub> nanodots<sup>20-22</sup> and Bi<sub>2</sub>Se<sub>3</sub> nanoplates<sup>23</sup> have been employed as CT CAs which are commonly used in clinical imaging. Moreover, BiNPs have received wide attention in the field of radiotherapy research due to their remarkable radiation dose enhancement under kilovolt-energy X-ray beams, which is significantly higher than the well-known gold radiation sensitizer.<sup>24</sup> As a direct thin-band-gap n-type semiconductor (1.3 eV), Bi<sub>2</sub>S<sub>3</sub> NPs with high near-infrared (NIR) absorption coefficient have been used as NIR absorbers to extend the absorption wavelength to the NIR region for the improvement of solar-harnessing capability of solar cells.<sup>25-28</sup> Encouraged

by the ideal NIR absorption property of BiNPs, it is very much possible to use them as CT agents, which thus makes them a simple but powerful precision nanomedicine that comprises only Bi<sub>2</sub>O<sub>3</sub> NPs without any additional functional components that can be used to simultaneously achieve CT bimodal imaging. However, it has been suggested that the significant radiosensitization effect of Bi<sub>2</sub>S<sub>3</sub> NPs could be successfully realized through their inhibition effect on tumor growth in a tumor-bearing mice model, where intrinsic potential biological toxicity of sulfur element could not be ignored.<sup>29</sup> Furthermore, as we have known, the lower cost of bismuth element and higher radiation dose enhancement<sup>30,31</sup> compared to gold element could make the BiNP a better candidate for further commercial use. Thus, it is suggested that Bi<sub>2</sub>O<sub>3</sub> NP can be used as an ideal alternative to evaluate the therapeutic effect of nanomedicine-based radiosensitizers in the interstitial radiotherapy research.

HA is a naturally linear polysaccharide and a major ligand due to its biocompatible, nontoxic, biodegradable, and non-immunogenic advantages. As a target-specific drug delivery carrier, HA has been investigated well in the HA receptor-mediated endocytosis because of its polyanionic characteristics and hydrophilicity,<sup>32</sup> and highly efficient targeted delivery to target sites with HA receptors, such as CD44, HARE, and LYVE-1, for various biological functions.<sup>33,34</sup>

According to over-mentioned intensive reports, we chose HA as a targeting ligand to synthesize the HA-Bi<sub>2</sub>O<sub>3</sub> NPs as a multifunctional theranostic platform that can afford spatial- and temporal-specific CT imaging and enable overcoming cancer radioresistance. This specifically developed tumor-targeted probe holds a great promise as a CT imaging CA with better CT imaging quality at reduced CA dosage when compared with the currently available CAs imaged using a clinical CT scanner. In order to exploit the attractive features of Bi element and that of multifunctional NPs, we evaluated the radiosensitizing effect of HA-Bi<sub>2</sub>O<sub>3</sub> NPs in hepatoma cells *in vitro* and tumor-bearing female mice model *in vivo*.

## Materials and methods

### Materials

Fluorescein diacetate (FDA) and propidium iodide (PI) were purchased from Sigma (St Louis, MO, USA). BiCl<sub>3</sub>·6H<sub>2</sub>O and diethylene glycol (99%) were acquired from Hengrui Pharmaceutical Co., Ltd (Lianyungang, People's Republic of China). 3-(4,5-Dimethyl-thiazol-2-yl)-5-(3-carboxymethoxyphenyl)-2-(4-sulfophenyl)-2H-tetrazolium (MTS) was purchased from Promega (Cell Titer Aqueous One Solution Cell Proliferation Assay kit; Madison, WI, USA).

NaH<sub>2</sub>PO<sub>4</sub>, Na<sub>2</sub>HPO<sub>4</sub>, and H<sub>2</sub>SO<sub>4</sub> were obtained from Guangfu Fine Chemical Research Institute (Tianjin, People's Republic of China). Fetal bovine serum and Dulbecco's Modified Eagle's Medium (DMEM) were purchased from Invitrogen China Limited (Shanghai, People's Republic of China). All chemicals were of analytical grade and were utilized without further purification.

### Synthesis of HA-Bi<sub>2</sub>O<sub>3</sub> NPs

The HA-Bi<sub>2</sub>O<sub>3</sub> NPs were prepared using a slightly modified procedure of the "polyol" method developed by Petoral et al.<sup>35</sup> Specifically, 5.7 mmol BiCl<sub>3</sub> was dissolved in 30 mL of diethylene glycol (DEG) and constantly stirred to form a transparent viscous solution. The solution was heated in a silicon oil bath at 140°C–160°C for 1 h. Then, 7.5 mmol NaOH dissolved in 30 mL of DEG was added. After complete dissolution of the reactants, the solution was refluxed at 180°C for 30 min under vigorous stirring. The prepared NPs were cooled to room temperature. Subsequently, 0.5 mmol HA and 0.5 mmol NaOH were added. The solution was then refluxed at room temperature for 6 h under strong stirring, yielding a white precipitate. After the system was cooled to room temperature naturally, the transparent suspension was filtered with a 0.22-μm membrane to remove any large-sized agglomerates. The prepared solution was then dialyzed against water for 3 days in a 14-kDa molecular weight cutoff dialysis bag. The dialysis solution was collected and freeze-dried using a vacuum freeze dryer. Thus, HA-Bi<sub>2</sub>O<sub>3</sub> NPs powders were obtained and stored for further characterization.

### Instrumentation and characterizations

The chemical structures of HA-Bi<sub>2</sub>O<sub>3</sub> NPs were analyzed using a Fourier transform infrared (FT-IR) spectrometer (Nicolet Nexus 470; GMI, Franklin, IN, USA). The elemental composition was determined by elemental analysis performed using X-ray photoelectron spectroscopy (XPS). The resultant particle sizes were analyzed by a NanoDLS particle size analyzer (Brookhaven Instruments Corporation, Holtsville, NY, USA). The morphologies of the HA-Bi<sub>2</sub>O<sub>3</sub> NPs were examined by high-resolution transmission electron microscopy (HRTEM) on a JEM-2100 microscope (JEOL, Tokyo, Japan) under an accelerating voltage of 200 kV. Ultraviolet–visible (UV–Vis) absorption spectra were recorded using a UV-2450 UV–Vis spectrophotometer (Shimadzu, Kyoto, Japan). Photoluminescence emission measurement was made using a Cary Eclipse Fluorometer (Varian, Palo Alto, CA, USA). The bismuth element of HA-Bi<sub>2</sub>O<sub>3</sub> NPs was quantified by linear calibration using amounts of potassium iodine

previously determined by inductively coupled plasma mass spectroscopy (ICP-MS).

### Cellular binding and uptake tests

For cellular binding and uptake analysis, each cell line (1×10<sup>6</sup> cells) was treated with phosphate-buffered saline (PBS) (pH 7.4) containing 2% bovine serum albumin at 4°C for 30 min. The cells were then washed three times with PBS (pH 7.4), followed by an incubation with fluorescein isothiocyanate (FITC)-labeled HA-Bi<sub>2</sub>O<sub>3</sub> NPs (5 mg/mL) at 37°C for 6 h. To remove unbound NPs, the cells were washed three times with and resuspended in PBS (pH 7.4). The cellular binding of HA-Bi<sub>2</sub>O<sub>3</sub> NPs was analyzed using flow cytometry on a FACS calibur cytometer (BD Accuri™ C6; BD Biosciences, Becton, Dickinson and Company, Franklin Lakes, NJ, USA). In order to observe the effect of free HA on cellular uptake, the cells were also treated with free HA (5 mg/mL) at 37°C for 1 h, prior to their incubation with FITC-labeled HA-Bi<sub>2</sub>O<sub>3</sub> NPs.

### Cell viability assay of the HA-Bi<sub>2</sub>O<sub>3</sub> NPs

The cytotoxicity of HA-Bi<sub>2</sub>O<sub>3</sub> NPs was evaluated in T/G HA-VSMC (aorta/smooth muscle, ATCC® number: CRL-1999), MCF7 (mammary gland, breast, derived from metastatic site: pleural effusion, ATCC® number: HTB-22™), and SMMC-7721 (human hepatocarcinoma, ATCC® number: HB-8065) cells using the MTS assay according to the protocol supplied by the manufacturer. Briefly, these cells were seeded in a 96-well plate at a density of 3×10<sup>3</sup> cells/well<sup>36</sup> and incubated for 24 h at 37°C and 5% CO<sub>2</sub>, and then the growth medium was replaced with DMEM containing different concentrations of HA-Bi<sub>2</sub>O<sub>3</sub> NPs. Each sample was prepared in triplicate. After incubation for 24 h, 20 μL MTS solution was added to each well and incubated for 3 h at 37°C under 5% CO<sub>2</sub>. The absorbance of each well was measured at 490 nm using Synergy HT Multi-Mode Microplate Reader (BioTek, Winooski, VT, USA). Non-seeded wells (containing only DMEM) were used as zero sitting, non-treated cells (in DMEM) were used as control, and the relative cell viability (mean ± SD, n=3) was expressed as (Abs sample – Abs zero sitting)/(Abs control – Abs zero sitting) × 100%.

### Hemolysis assay

All animal experiments in this study were executed according to the protocol approved by the Management Rules of the Ministry of Health of the People's Republic of China and approved by the Institutional Animal Care and Use Committee of Jiangsu University. Hemolysis assay was carried out in accordance with the procedure reported in

the literature<sup>37–39</sup> with slight modification. In brief, fresh mouse blood stabilized with heparin sodium was kindly prepared. The blood was centrifuged (1,200 rpm, 15 min) to remove supernatant, washed with PBS five times to completely remove serum, and obtain the mouse red blood cells (MRBCs). Thereafter, the diluted MRBC suspension (0.1 mL) was transferred into 2 mL tubes prefilled with 0.9 mL ddH<sub>2</sub>O (as positive control), 0.9 mL PBS (as negative control), and 0.9 mL PBS containing HA-Bi<sub>2</sub>O<sub>3</sub> NPs with different particle concentrations (25–800 µg/mL), respectively. The mixtures were incubated for 2 h at 37°C after gentle shaking and centrifuged at 12,000 rpm for 1 min. Finally, the photographs of the samples were taken, and the absorbance of the supernatants (hemoglobin) was measured by a UV-2450 UV–Vis spectrophotometer. The hemolysis percentages of different samples were calculated by dividing the difference in absorbance at 541 nm.

## Histological analysis

Mice were sacrificed 30 days after intravenous injection of HA-Bi<sub>2</sub>O<sub>3</sub> NPs at a dose of 40 mg/kg, and mice without the injection of HA-Bi<sub>2</sub>O<sub>3</sub> NPs were used as control. Susceptible tissues (heart, spleen, liver, lung, and kidney) were harvested from the above two groups (control and test groups). The organs were immersed in 4% paraformaldehyde for 24 h at 4°C, dehydrated, and treated for inclusion in paraffin. The specimen was sectioned serially at 4-mm thickness, stained with hematoxylin and eosin, and observed under an optical microscope.

## Biodistribution of HA-Bi<sub>2</sub>O<sub>3</sub> NPs in vivo

To study the biodistribution of HA-Bi<sub>2</sub>O<sub>3</sub> NPs in vivo, the HA-Bi<sub>2</sub>O<sub>3</sub> NPs solution (40 mg/kg) in PBS was injected into ICR mice via the tail vein. After 24 h postadministration, mice were sacrificed, and organs were dissected and weighed. For ICP-MS assay, each sample was added to 5 mL of H<sub>2</sub>NO<sub>3</sub>, transferred to flasks, and sealed for predigestion overnight. Then, 3 mL of 30% H<sub>2</sub>O<sub>2</sub> was added to each flask. The flasks were heated at 120°C for 2 h and then cooled to room temperature. A series of Bi<sup>+</sup> standard solutions (0, 0.5, 1.5, 10, 50, and 100 ppb) were prepared with the above solution. Both standard and test solutions were measured by ICP-MS. The amount of Bi elements was finally normalized to the cell number or tissue weight per gram.

## Live–dead staining assay and flow cytometry

To study the radiosensitization effect of HA-Bi<sub>2</sub>O<sub>3</sub> NPs, SMMC-7721 cells were seeded in six-well plates at a density

of 4.0×10<sup>4</sup> cells/well and allowed to grow for 12 h and divided into six groups (control, HA-Bi<sub>2</sub>O<sub>3</sub> NPs, radiation, radiation +50 µg/mL HA-Bi<sub>2</sub>O<sub>3</sub> NPs, radiation +100 µg/mL HA-Bi<sub>2</sub>O<sub>3</sub> NPs, and radiation +200 µg/mL HA-Bi<sub>2</sub>O<sub>3</sub> NPs). When cells had grown to 80% in plates, the first group received no treatment, the second one was incubated with 200 µg/mL HA-Bi<sub>2</sub>O<sub>3</sub> NPs for 24 h, the third one was just irradiated at 6 Gy, and the fourth to sixth ones were irradiated at 6 Gy, and at the same time, incubated with different concentrations of HA-Bi<sub>2</sub>O<sub>3</sub> NPs (50, 100, and 200 µg/mL) for 24 h, respectively. After that, FDA and PI working buffer was added for cell staining. The fluorescence of stained cells was observed under a fluorescence microscope; live cells showed green color, and dead ones exhibited red color.

Furthermore, cells treated by different treatments were washed three times with PBS, digested, collected, and centrifuged at a speed of 2,000 rpm for 5 min, and then fixed with 70% ethanol at –20°C overnight followed by PI staining. DNA fragmentation was quantified by the fluorescence intensity of PI on a Beckman Coulter Epics XL MCL flow cytometer (BD Accuri C6) and analyzed by software (Flowjo 7.6.2) to clearly understand the cell cycle distribution and apoptosis.

## Clonogenic survival assays

Cells were seeded in six-well plates at a density of 1.0×10<sup>3</sup> cells/well and permitted to grow for 16 h. The cells were incubated with 200 µg/mL HA-Bi<sub>2</sub>O<sub>3</sub> NPs diluted in cell culture medium for 6 h. The cells were then irradiated at 6 Gy. After irradiation, cells were allowed to grow for 14 days, fixed with 4% paraformaldehyde at room temperature for 40 min, and stained with 1% crystal violet after washing the cells. Cells were treated on a clinical linear accelerator (Oncor, Dallas, TX, USA) with 6 MV irradiation under a radiation field of 10×10 cm at a source-to-skin distance (SSD) of 100 cm to cover the entire cells.

## In vivo and in vitro CT imaging study and biodistribution of HA-Bi<sub>2</sub>O<sub>3</sub> NPs

In vitro and in vivo CT images were acquired on a clinical 64-slice multidetector CT scanner (SOMATOM Emotion; Siemens, Munich, Germany). To study the CT images in vitro, the solutions of HA-Bi<sub>2</sub>O<sub>3</sub> NPs with different concentrations ranging from 0 to 10 mg/mL were added to a 96-well culture plate, using the commercial contrast Omnipaque (GE Healthcare (Shanghai) Co., Ltd., Shanghai, People's Republic of China) as control. The X-ray attenuation intensity was evaluated with the average values of gray density by the corresponding software (ImageJ) and medical image analysis system. For CT imaging in vivo, we choose the normal ICR mice as model.

Animal experiments were performed strictly following the Animal Management Rules of the Ministry of Health of the People's Republic of China. HA-Bi<sub>2</sub>O<sub>3</sub> NPs (40 mg/kg) filtered through sterilized membrane filters (pore size 0.22 μm) were intravenously injected into the animals before investigating with a CT scanner. These samples for CT imaging in vitro and animals in vivo were imaged with the following parameters: tube voltage, 130 kV; current intensity, 180 mA; slice thickness, 5.0 mm; and scan time, 2.85 s. The corresponding dissected organs were treated with microwave digestion.

## Therapeutic evaluation of HA-Bi<sub>2</sub>O<sub>3</sub> NPs in tumor-bearing mice

Female ICR mice with body weights of 19–21 g and aged 6 weeks were obtained from Jiangsu University Laboratory Animal Center (No 201602201) and placed under the standard conditions (20°C±2°C room temperature, 60%±10% relative humidity). Animals were acclimatized to this environment for 5 days prior to treatment. Animal experiments were consistent with the Animal Management Rules of the Ministry of Health of the People's Republic of China (SCXK(s) 2013-0011).

The technology of establishing the animal models with Herps cells is very mature.<sup>40</sup> Animal models were established by the following procedures: First, 1×10<sup>6</sup> Herps cells were inoculated into mice intraperitoneally, and the ascites were collected after 5 days. Then, these ascites were injected subcutaneously at an SSD of 100 cm. When the tumor sizes reached ~100 mm<sup>3</sup>, subcutaneous tumors models were

established and applied to the following experiments. To establish in situ tumor model, the tumor-bearing mice were sacrificed, and subcutaneously, tumors were dissected out. These solid tumors were cut into small pieces and inoculated into normal mice liver in situ. Five days post-inoculation, in situ tumor models were established.

Mice bearing subcutaneous tumors were treated with radiation at 3 Gy per fraction at a total dose of 30 Gy within 10 days. The radiotherapy was conducted after 3 h of intravenous injection of HA-Bi<sub>2</sub>O<sub>3</sub> NPs (10 mg/kg), on a Siemens Primus clinical linear accelerator (6 MeV) using a radiation field of 10×10 cm to cover the entire tumor. Tumor growth and mouse weight were measured in the following days. The tumor sizes were measured by a caliper and calculated as follows:  $V = ab^2/2$ , where  $V$  (mm<sup>3</sup>) is the volume of the tumor, and  $a$  (mm) and  $b$  (mm) are the tumor length and tumor width, respectively. Relative tumor volumes were normalized to their initial sizes. Each group contained eight mice and statistical analysis was performed using Student's two-tailed  $t$ -test ( $P < 0.05$ ,  $P < 0.001$ ).

## Results and discussion

### Preparation and characterization of HA-Bi<sub>2</sub>O<sub>3</sub> NPs

The HA-Bi<sub>2</sub>O<sub>3</sub> NPs were successfully fabricated according to the illustrated diagram in Figure 1. In this study, the morphological examination was carried out by TEM, and the resultant particle sizes were analyzed by NanoDLS particle size analyzer. As shown in Figure 2A and B, TEM/HRTEM

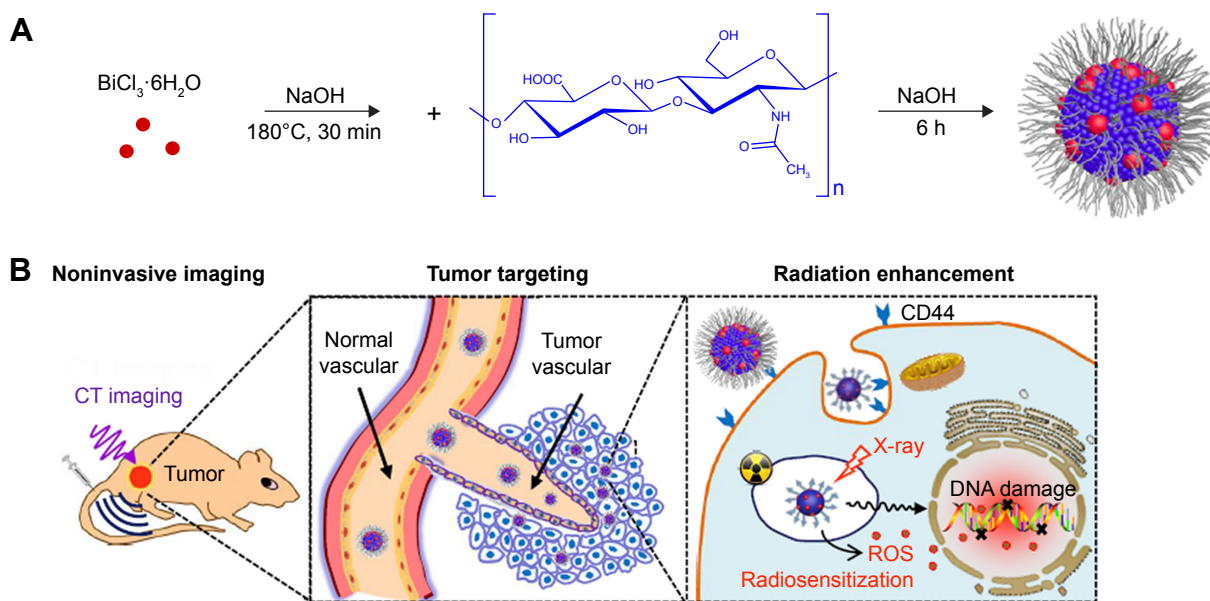


**Figure 1** (A) Schematic synthesis of HA-Bi<sub>2</sub>O<sub>3</sub> NPs by pyrolysis method and (B) the following biomedical applications.

**Abbreviations:** HA-Bi<sub>2</sub>O<sub>3</sub> NPs, hyaluronic acid-functionalized bismuth oxide nanoparticles; ROS, reactive oxygen species; CT, computed tomography.

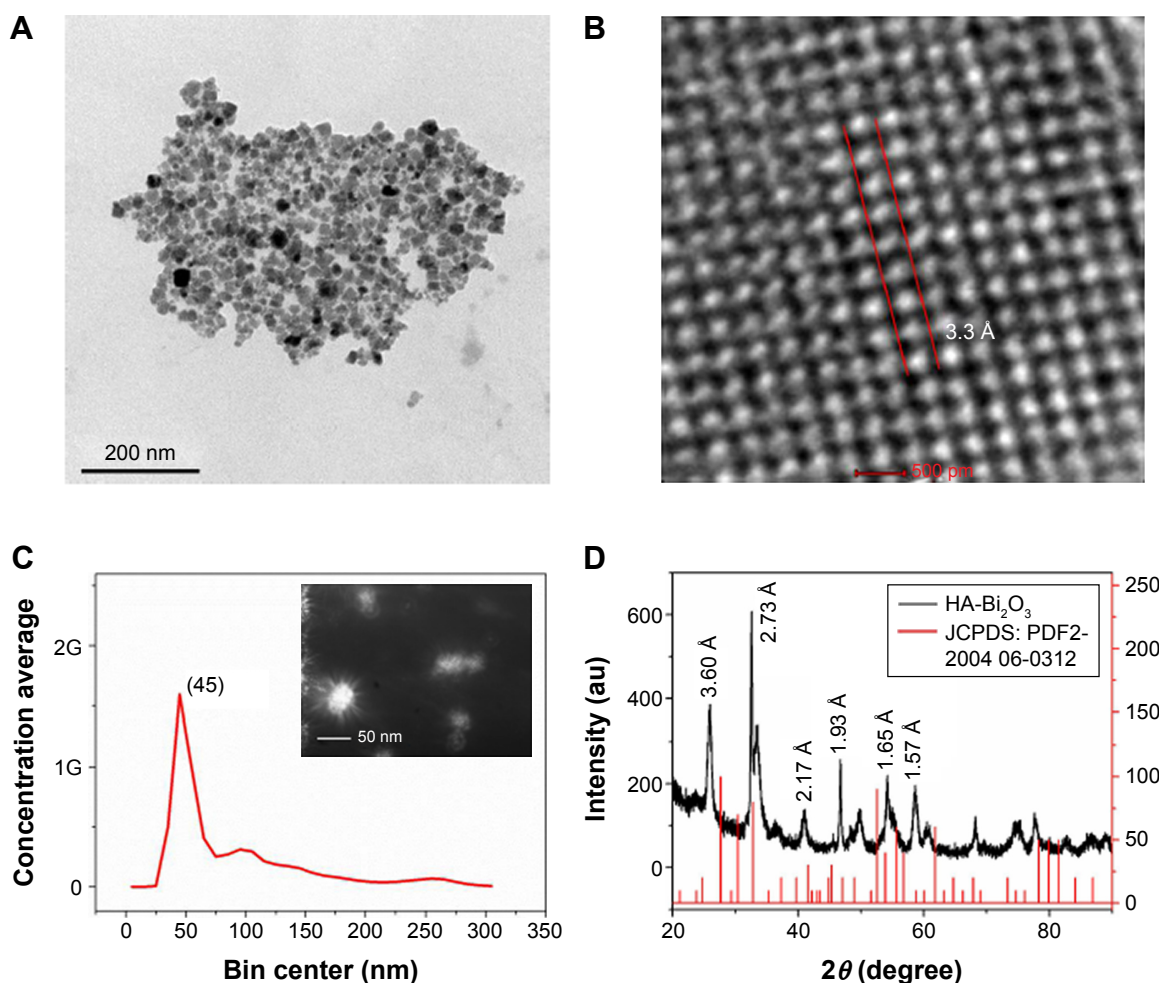


**Figure 2** (A) TEM image of HA-Bi<sub>2</sub>O<sub>3</sub> NPs. (B) HRTEM image of HA-Bi<sub>2</sub>O<sub>3</sub> NPs. (C) Size distribution of HA-Bi<sub>2</sub>O<sub>3</sub> NPs. The inset shows the optical image of the HA-Bi<sub>2</sub>O<sub>3</sub> NPs. (D) XRD pattern of the HA-Bi<sub>2</sub>O<sub>3</sub> NPs.

**Abbreviations:** TEM, transmission electron microscopy; HA-Bi<sub>2</sub>O<sub>3</sub> NPs, hyaluronic acid-functionalized bismuth oxide nanoparticles; HRTEM, high-resolution transmission electron microscopy; XRD, X-ray diffraction; JCPDS: PDF, Joint Committee on Powder Diffraction Standards; powder diffraction file.

showed that the HA-Bi<sub>2</sub>O<sub>3</sub> NPs all exhibited uniform dispersion and discrete quasi-spherical shape without apparent aggregation. HA-Bi<sub>2</sub>O<sub>3</sub> NPs had a diameter of 45±0.6 nm and possessed a uniform lattice structure with a lattice fringe of interlayer spacing ( $d$ ) = 3.3±0.2 Å. Dynamic light scattering measurement showed that HA-Bi<sub>2</sub>O<sub>3</sub> NPs had uniform size distribution (Figure 2C). As shown in Figure S1, the average diameter of HA-Bi<sub>2</sub>O<sub>3</sub> NPs in aqueous solution was maintained stable with an average size of 50 nm for 8 days. The average size of HA-Bi<sub>2</sub>O<sub>3</sub> NPs in PBS solution remained at 47.4 nm on the first day. The average diameters of HA-Bi<sub>2</sub>O<sub>3</sub> NPs were slightly influenced and ranged from 47.4 to 53.7 nm for 8 days. Compared to normal tissues, capillary endothelial permeability of tumor tissues was increased, and the endothelial gap was between 100 and 600 nm.<sup>41</sup> Therefore, NPs with desirable size are beneficial to accumulate in the tumor tissues and dramatically improve the passive targeting drug delivery efficiency.

## Chemical structure and surface composition of the HA-Bi<sub>2</sub>O<sub>3</sub> NPs

Surface functional groups and composition of the HA-Bi<sub>2</sub>O<sub>3</sub> NPs were investigated using FT-IR spectrum and XPS pattern. FT-IR spectrum was obtained for both naked Bi<sub>2</sub>O<sub>3</sub> and HA-Bi<sub>2</sub>O<sub>3</sub> NPs (Figure S2). For the HA-Bi<sub>2</sub>O<sub>3</sub> NPs, the characteristic absorption bands of  $\nu_{as}$  O-C-O at 1,380 cm<sup>-1</sup> demonstrated the presence of carbonate groups. The broad peaks at 3,340 and 2,900 cm<sup>-1</sup> were attributed to the O-H and C-H stretching vibrations, respectively, which corresponded to the surface-adsorbed water. The stretching vibrations of  $\nu_{as}$  O-C-O were enhanced, indicating the introduction of carboxylic group of HA. These results showed that the functional groups of HA-Bi<sub>2</sub>O<sub>3</sub> NPs mainly contained certain plentiful C=O, -COOH, and -OH groups. The presence of these functional groups located at their surface endowed the HA-Bi<sub>2</sub>O<sub>3</sub> NPs with excellent

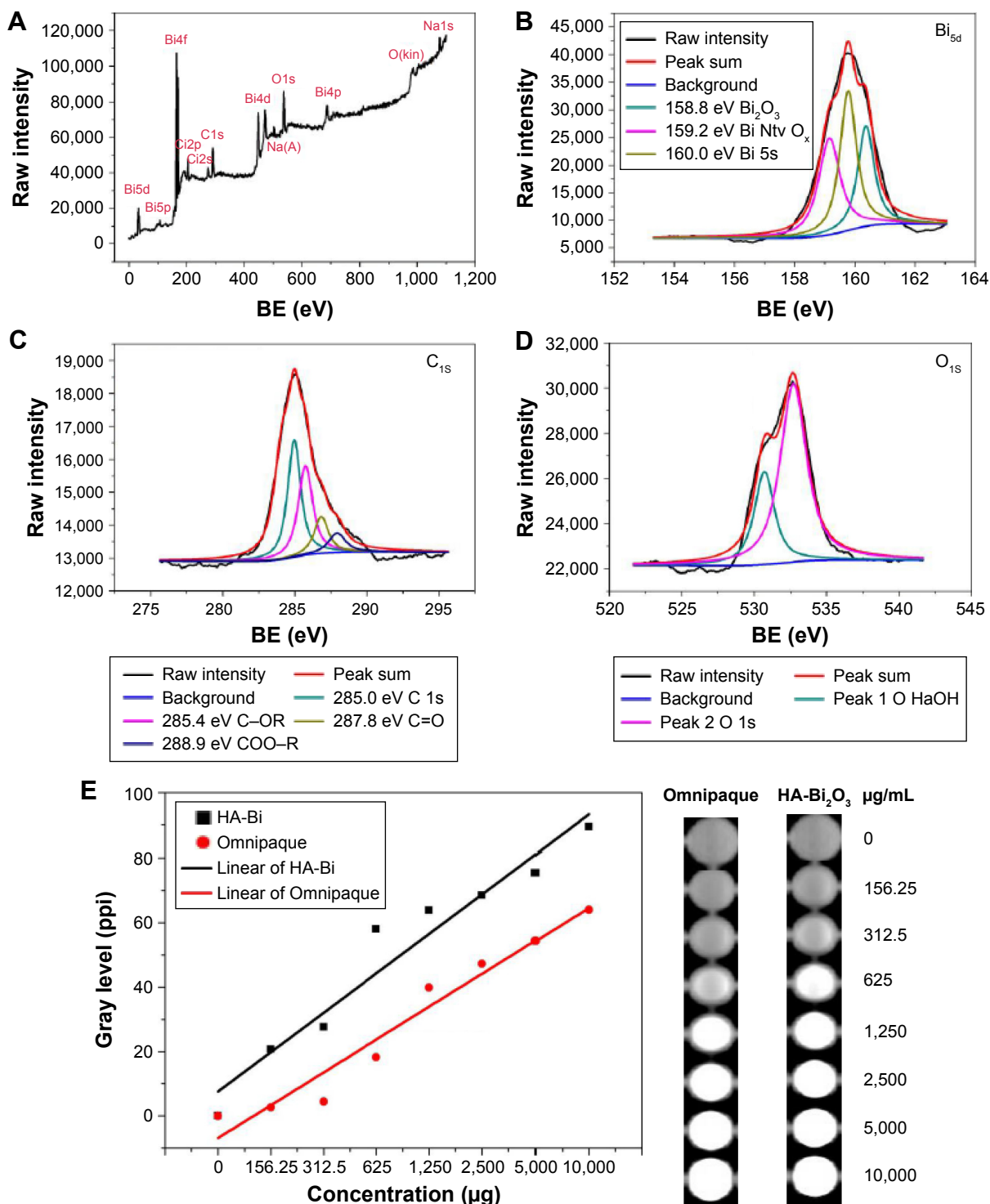


**Figure 3** XPS spectra of the HA-Bi<sub>2</sub>O<sub>3</sub> NPs. (A) Survey spectrum. (B) Bi<sub>5d</sub> spectrum. (C) C<sub>1s</sub> spectrum. (D) O<sub>1s</sub> spectrum. (E) CT images in PBS with different concentrations of HA-Bi<sub>2</sub>O<sub>3</sub> NPs and Omnipaque solution. Fitting curve of gray level.

**Note:** 1s, 2p, 2s, 4d, 4p, 4f, 5d, and 5p are azimuthal quantum numbers.

**Abbreviations:** XPS, X-ray photoelectron spectroscopy; HA-Bi<sub>2</sub>O<sub>3</sub> NPs, hyaluronic acid-functionalized bismuth oxide nanoparticles; CT, computed tomography; BE, binding energy; PBS, phosphate-buffered saline; Bi, bismuth; Adj R<sup>2</sup>, adjusted coefficient of determination.

hydrophilicity and dispersibility in water.<sup>42</sup> The survey XPS spectrum (Figure 3A) showed three typical peaks at 159.75, 285.1, and 532.65 eV, which indicated that the HA-Bi<sub>2</sub>O<sub>3</sub> NPs were mainly composed of bismuth, carbon, and oxygen

elements. The high-resolution spectrum of Bi<sub>5d</sub> (Figure 3B) revealed the presence of three strong peaks at 158.8, 159.2, and 160.0 eV with a spin-orbit splitting of 32 eV corresponding, respectively, to the Bi<sub>2</sub>O<sub>3</sub>, native oxide (Ntv Ox), and

1s energy levels of Bi. These observations were in good agreement with previous reports for Bi<sub>2</sub>O<sub>3</sub> NPs.<sup>43</sup> The C (1s) spectrum as shown in Figure 3C was dominated by four major peaks positioned at 285.0, 285.4, 287.8, and 531.8 eV, which corresponded, respectively, to the 1s, C–OR, C=O, and COO–R energy levels of C atom. The O (1s) spectrum as shown in Figure 3D was dominated by two major peaks positioned at 530.5 and 531.8 eV, which corresponded to the bond between O (NaOH) and O (1s).

The crystal structure of the HA-Bi<sub>2</sub>O<sub>3</sub> NPs was investigated by X-ray diffraction. As shown in Figure 2D, there were diffraction peaks in the HA-Bi<sub>2</sub>O<sub>3</sub> NP pattern around 24.710° ( $d=0.360$  nm, grade of tolerance [hkl]=220 plane), 32.778° ( $d=0.273$  nm, hkl=321 plane), 41.583° ( $d=0.217$  nm, hkl=332 plane), 47.045° ( $d=0.193$  nm, hkl=311 plane), 55.658° ( $d=0.165$  nm, hkl=610 plane), 58.763° ( $d=0.157$  nm, hkl=621 plane), and other crystal planes, which corresponded to the characteristic peaks of  $\alpha$ -Bi<sub>2</sub>O<sub>3</sub> (monoclinic system), respectively. The corresponding  $d$  was calculated according to the Bragg's law (the wavelength of Cu-K $\alpha$  is 0.154 nm). These diffraction peaks matched well with the characteristic peaks of cubic Bi<sub>2</sub>O<sub>3</sub> (JCPDS 2004 06-0312).

## X-ray attenuation capacity of the HA-Bi<sub>2</sub>O<sub>3</sub> NPs

We then investigated the X-ray attenuation capacity of the HA-Bi<sub>2</sub>O<sub>3</sub> NPs compared with the Omnipaque (commercial CT CAs). As shown in Figure 3E, the CT image brightness increased with the HA-Bi<sub>2</sub>O<sub>3</sub> NPs concentration, which was similar to the behavior of the Omnipaque solution. At the HA-Bi<sub>2</sub>O<sub>3</sub> NP concentration of 156.25 to 1×10<sup>4</sup>  $\mu$ g/mL, the mean gray values were 137.3 (156.25  $\mu$ g/mL), 167.6 (312.5  $\mu$ g/mL), 173.5 (625  $\mu$ g/mL), 178.1 (1.25×10<sup>4</sup>  $\mu$ g/mL), 185.1 (2.5×10<sup>3</sup>  $\mu$ g/mL), and 199.1 (1×10<sup>4</sup>  $\mu$ g/mL); at the Omnipaque concentration of 156.25 to 1×10<sup>4</sup>  $\mu$ g/mL, the mean gray values were 114.1 (156.25  $\mu$ g/mL), 127.9 (312.5  $\mu$ g/mL), 149.5 (625  $\mu$ g/mL), 156.9 (1.25×10<sup>4</sup>  $\mu$ g/mL), 164.0 (2.5×10<sup>3</sup>  $\mu$ g/mL), and 173.7 (1×10<sup>4</sup>  $\mu$ g/mL). The CT image of HA-Bi<sub>2</sub>O<sub>3</sub> NPs was much brighter than that of Omnipaque under the same dosage of radiation. Further quantitative analysis data showed that X-ray attenuation intensity of both HA-Bi<sub>2</sub>O<sub>3</sub> NPs and the Omnipaque increased with the mass concentration of radiodense element. Nevertheless, the HA-Bi<sub>2</sub>O<sub>3</sub> NPs exhibited much higher X-ray attenuation capacity than Omnipaque under the same radioactive element concentrations ( $\geq 156.25$   $\mu$ g/mL). The superior X-ray attenuation performance endowed HA-Bi<sub>2</sub>O<sub>3</sub> with ideal CT

imaging capacity for identifying accurate localization of tumor tissue.

## Cellular binding and phagocytosis tests

The HA-Bi<sub>2</sub>O<sub>3</sub> NPs uptake by cells were quantitatively evaluated using flow cytometry method. Cells were incubated with 100  $\mu$ g/mL of the HA-Bi<sub>2</sub>O<sub>3</sub> NPs for 6 h. Ten thousand cells were collected and analyzed by flow cytometry (Figure 4A and B). The single-color histograms indicated that the number of cells labeled by FITC-modified HA-Bi<sub>2</sub>O<sub>3</sub> NPs was 97.66% (SMMC-7721) and 86.64% (MCF7), respectively. The results validated that HA-Bi<sub>2</sub>O<sub>3</sub> NPs were readily internalized by cancer cells.

In order to verify the HA receptor-mediated cellular uptake behavior, SMMC-7721 (CD44 high-expression cell line) and MCF7 cells (CD44 low-expression cell line) were pretreated with free HA before incubation with HA-Bi<sub>2</sub>O<sub>3</sub> NPs. As previously reported,<sup>44–46</sup> relative expression of CD44 in SMMC-7721 was higher than in MCF7 according to real-time PCR results; relative expression of CD44 in MCF7 was only 25.6% of the expression in SMMC-7721 (Figure S3). From flow cytometry assay, it was found that the amount of HA-Bi<sub>2</sub>O<sub>3</sub> uptake by SMMC-7721 cells (93.94%) was more than that of MCF7 cells (85.90%) (Figure 4C and D). As expected, the uptake of HA-Bi<sub>2</sub>O<sub>3</sub> NPs was reduced to 68.19% in SMMC-7721 cells, but a slight change (75.88%) in MCF7 cells was observed when the two cell lines were pretreated simultaneously with free HA. Free HA was able to bind to CD44 and inhibited the binding of HA-Bi<sub>2</sub>O<sub>3</sub> to CD44 competitively; the influence of free HA on SMMC-7721 was noticeable because relative expression of CD44 in SMMC-7721 cells was higher than in MCF7 cells. These results suggest that HA-Bi<sub>2</sub>O<sub>3</sub> NPs could be effectively taken up through the HA receptor-mediated endocytosis. It was also worthy of note that SMMC-7721 cells exhibited much higher uptake of HA-Bi<sub>2</sub>O<sub>3</sub> NPs than MCF7 cells, implying the synergistic effect of CD44 on cellular internalization of HA-Bi<sub>2</sub>O<sub>3</sub> NPs.

In addition, we further employed confocal laser scanning microscopy to observe the intracellular distribution of FITC-labeled HA-Bi<sub>2</sub>O<sub>3</sub> NPs in SMMC-7721 and MCF7 cells stained with LysoTracker Red DND-26 probe. Figure 4E shows that HA-Bi<sub>2</sub>O<sub>3</sub> NPs with green fluorescence exhibited a colocalization in the lysosomes with red fluorescence. Based on the data, we could speculate that HA-Bi<sub>2</sub>O<sub>3</sub> NPs may be preferably internalized into the lysosomes after receptor-mediated endocytosis. More importantly, the green fluorescence was more noticeable in SMMC-7721 than in MCF7. Because free



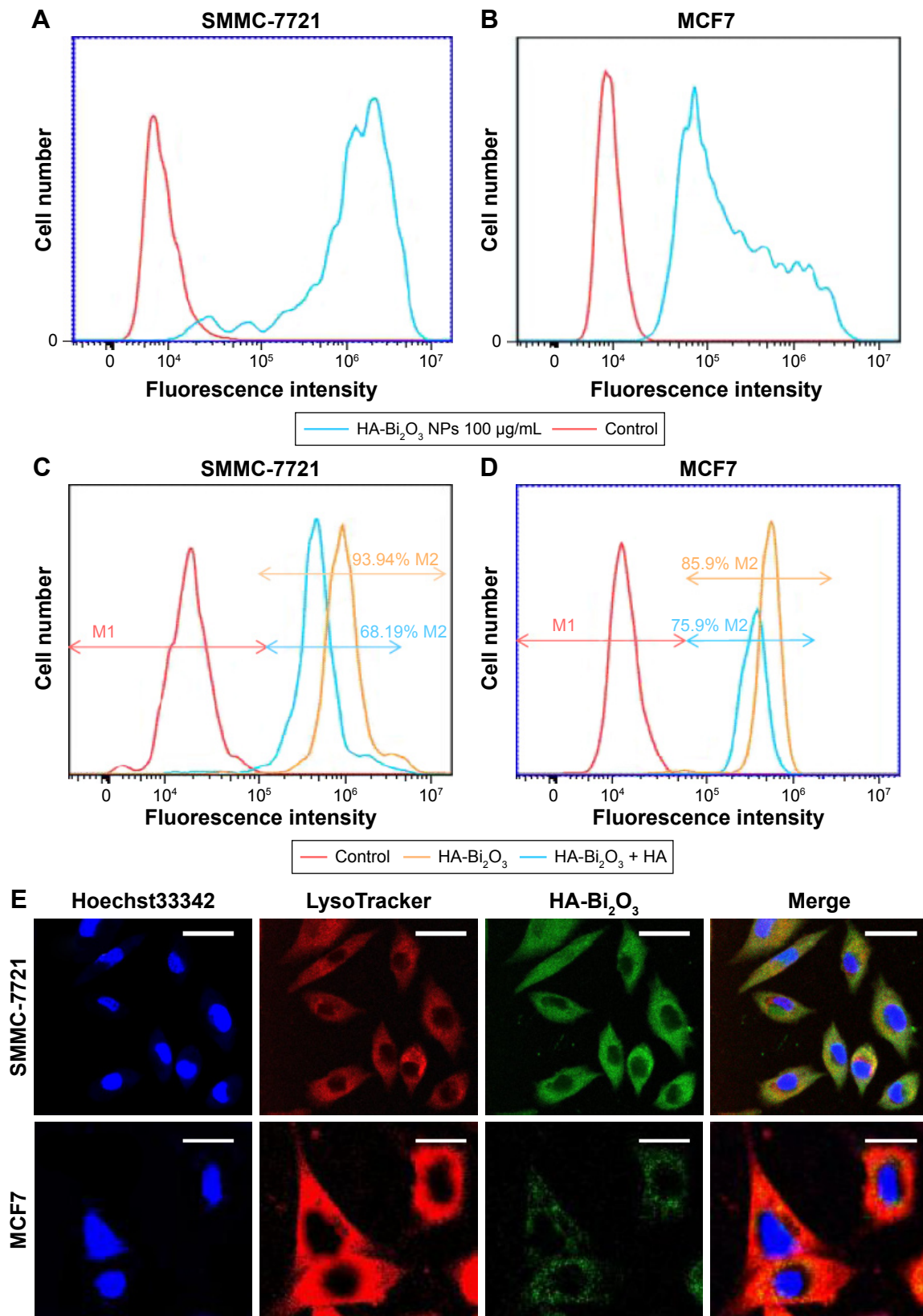


**Figure 4** (A and B) Fluorescence signal intensity of SMMC-7721 and MCF7 cells incubated with FITC-HA-Bi<sub>2</sub>O<sub>3</sub> NPs (through FL1). (C and D) The effect of free HA on the fluorescence signal intensity of SMMC-7721 and MCF7 cells after incubation with FITC-labeled HA-Bi<sub>2</sub>O<sub>3</sub> NPs. (E) Fluorescence images of SMMC-7721 (scale bars =20 µm) and MCF7 (scale bars =10 µm) cells after exposure to HA-Bi<sub>2</sub>O<sub>3</sub> NPs. Cells were stained with Hoechst33342 and LysoTracker. HA-Bi<sub>2</sub>O<sub>3</sub> NPs were modified with FITC. **Abbreviations:** FITC, fluorescein isothiocyanate; FITC-HA-Bi<sub>2</sub>O<sub>3</sub> NPs, FITC-labeled HA-Bi<sub>2</sub>O<sub>3</sub> NPs; HA, hyaluronic acid; HA-Bi<sub>2</sub>O<sub>3</sub> NPs, HA-functionalized bismuth oxide nanoparticles.

HA can compete with CD44 binding, HA-Bi<sub>2</sub>O<sub>3</sub> NPs were more easily internalized by SMMC-7721 cells than MCF7 cells, implying the synergistic effect of CD44 on cellular internalization of HA-Bi<sub>2</sub>O<sub>3</sub> NPs.

## Cytotoxicity and intracellular tracking of the HA-Bi<sub>2</sub>O<sub>3</sub> NPs

As potential biomedical agents, the HA-Bi<sub>2</sub>O<sub>3</sub> NPs are expected to possess good biocompatibility for their biomedical application. Firstly, the inherent cytotoxicity of HA-Bi<sub>2</sub>O<sub>3</sub> NPs was assessed in MCF7, SMMC-7721, and VSMC cells via MTS assay. As shown in Figure 5A, all the HA-Bi<sub>2</sub>O<sub>3</sub> NPs at different concentrations exhibited negligible cytotoxicity. Even at the concentration of 400 µg/mL and with 24-h exposure time, the cell viability was ~90%. Second, the hemocompatibility of the HA-Bi<sub>2</sub>O<sub>3</sub> NPs in vitro was estimated using hemolysis assay. As shown in Figures 5B and S4, we obviously found the hemolysis of red blood cells in the positive control. On the contrary, no

obvious hemolysis phenomenon was observed after incubation with different concentrations from 12.5 to 400 µg/mL for 2 hours administration, which was similar to the negative normal saline. Compared to the negative control, the percentage of hemolysis at different concentration of HA-Bi<sub>2</sub>O<sub>3</sub> NPs was quantitatively evaluated based on the absorbance the supernatant at 541 nm. The results showed that the hemolysis percentages of the HA-Bi<sub>2</sub>O<sub>3</sub> NPs were all less than 7% in the studied concentration range from 25 to 800 µg/mL, which verified their favorable hemocompatibility. These results clearly indicated that the as-synthesized HA-Bi<sub>2</sub>O<sub>3</sub> NPs had very low cytotoxicity and good hemobiocompatibility.

## Biodistribution and histocompatibility of the HA-Bi<sub>2</sub>O<sub>3</sub> NPs in vivo

To further investigate whether HA-Bi<sub>2</sub>O<sub>3</sub> NPs could induce adverse effects (such as tissue damage, inflammation, or lesions) in the long term postinjection, we carried out a

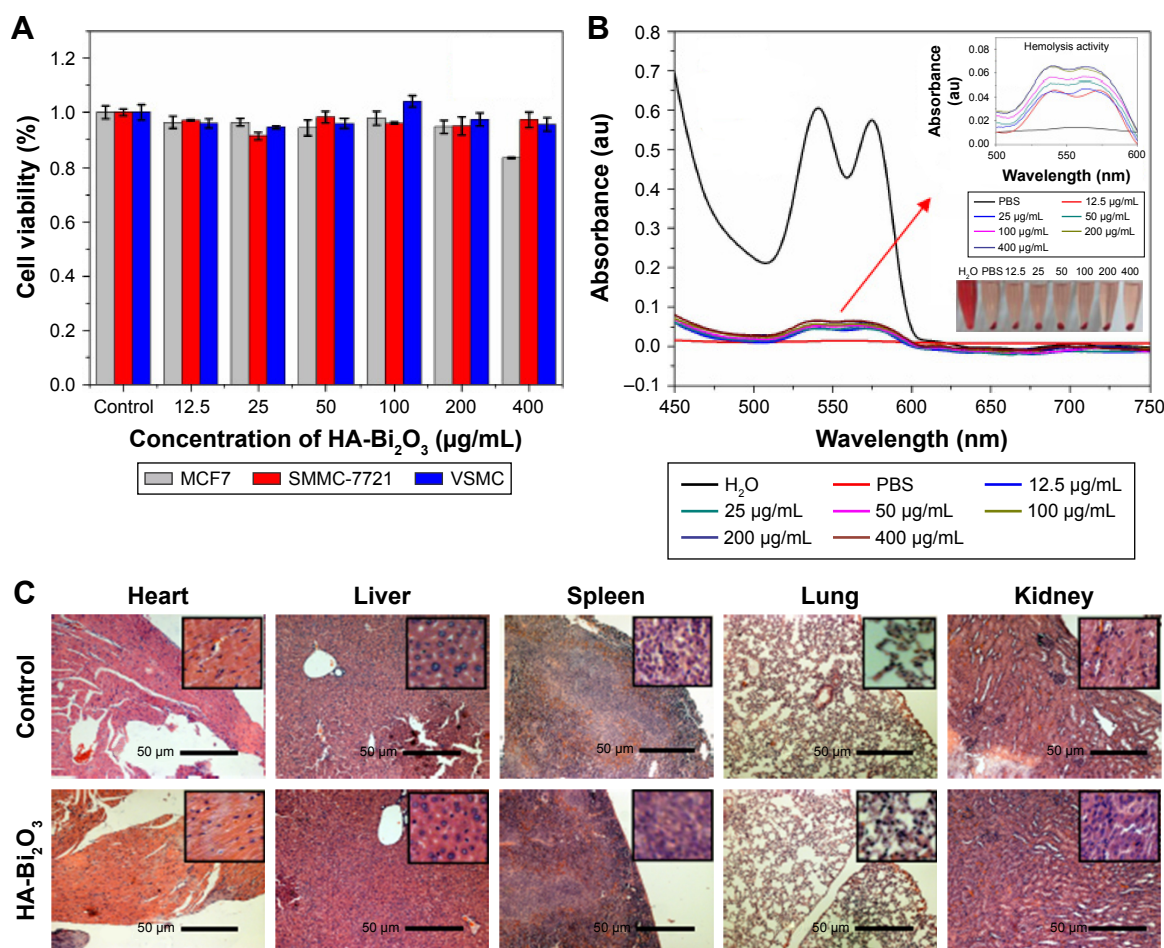


**Figure 5** (A) The effect of HA-Bi<sub>2</sub>O<sub>3</sub> NPs concentration on the viability of MCF7, SMMC-7721, and VSMC cells. (B) Hemolysis activity of the HA-Bi<sub>2</sub>O<sub>3</sub> NPs at different concentrations. PBS and water treatment were used as negative and positive controls, respectively. Arrow represents fractionated gain. (C) The H&E images of major organs after tail intravenous injections of HA-Bi<sub>2</sub>O<sub>3</sub> NPs. Scale bars = 50 µm.

**Abbreviations:** HA-Bi<sub>2</sub>O<sub>3</sub> NPs, hyaluronic acid-functionalized bismuth oxide nanoparticles; PBS, phosphate-buffered saline.

histological assessment of the susceptible organs of the mice (liver, heart, spleen, lung, and kidney) 30 days post-administration. As shown in Figure 5C, no obvious adverse effect associated with the administration of the HA-Bi<sub>2</sub>O<sub>3</sub> NPs was observed compared with the control group. The ICP-MS (Figure S5) results reported that the HA-Bi<sub>2</sub>O<sub>3</sub> NPs presented more appreciable accumulation in the liver (27.80 μg/g) than in the heart (4.83 μg/g), lung (2.10 μg/g), spleen (6.17 μg/g), and kidney (7.40 μg/g). However, the *in vivo* toxicity assessment profiles confirmed that the liver was unaffected by the accumulation of HA-Bi<sub>2</sub>O<sub>3</sub> NPs at least in the long term. These preliminary results proved that HA-Bi<sub>2</sub>O<sub>3</sub> NPs at the given dose hardly caused *in vivo* toxicity effects in the long term post-administration.

### Tumor-targeted CT imaging

The possibility of using HA-Bi<sub>2</sub>O<sub>3</sub> NPs as CAs for CT imaging *in vivo* was studied using Cancer Research mice (ICR mice) as a model (Figure S6). After intravenous injection of HA-Bi<sub>2</sub>O<sub>3</sub> NPs at a dose of 20 mg/kg, the CT images were acquired through different scan times. Figure 5A and B shows that HA-Bi<sub>2</sub>O<sub>3</sub> NPs exhibited gradual increases of CT signal intensities in tumor within 10 min. Compared with preinjection, a great contrast enhancement in tumor was observed clearly, indicating that HA-Bi<sub>2</sub>O<sub>3</sub> NPs caused a time-dependent increase of signals and exhibited a strong CT imaging capability at 10 min postinjection. Figure 6A and B also shows that the signal in both the kidney and bladder strongly increased at 30 min postinjection, which indicated the effective clearance of HA-Bi<sub>2</sub>O<sub>3</sub> NPs from the body via

renal metabolism. These results were further confirmed through CT transverse scans at different levels.

### Radiosensitization of HA-Bi<sub>2</sub>O<sub>3</sub> NPs *in vitro*

Previous studies have demonstrated that heavy metal-based radiosensitizers could absorb high-energy photons and emit secondary electrons and Auger electrons, which trigger a series of biological and chemical effects, such as destruction of DNA, proteins, and other intracellular components.<sup>47,48</sup> The therapeutic effectiveness of radiotherapy could not be realized completely due to inaccurate localization and inherent radioresistance of tumors. To address these limits, the excellent performance of HA-Bi<sub>2</sub>O<sub>3</sub> NPs as CAs *in vitro* has encouraged us to perform an *in vivo* experiment to investigate whether its potential could be applied to improve spatial localization accuracy for X-ray CT in radiosensitization of tumors. Firstly, cell counting kit-6 (cck8) assay was conducted to explore whether any dose enhancement was caused by this combination treatment. As depicted in Figure 7A, HA-Bi<sub>2</sub>O<sub>3</sub> NPs-only (concentration ranging from 0 to 400 μg/mL) treatment had no significant influence on the SMMC-7721 cell viability, and X-ray (ranging from 0 to 9 Gy) irradiation treatment decreased the SMMC-7721 cell viability to 45% at 9 Gy. Especially, the combination of X-ray irradiation with HA-Bi<sub>2</sub>O<sub>3</sub> NPs dramatically decreased the SMMC-7721 cell viability to <25% with the concentration of 200 μg/mL at 6 Gy. Next, clonogenic assay in SMMC-7721 cells was conducted to evaluate the change in cell viability caused by the combination treatment of X-ray irradiation and HA-Bi<sub>2</sub>O<sub>3</sub>

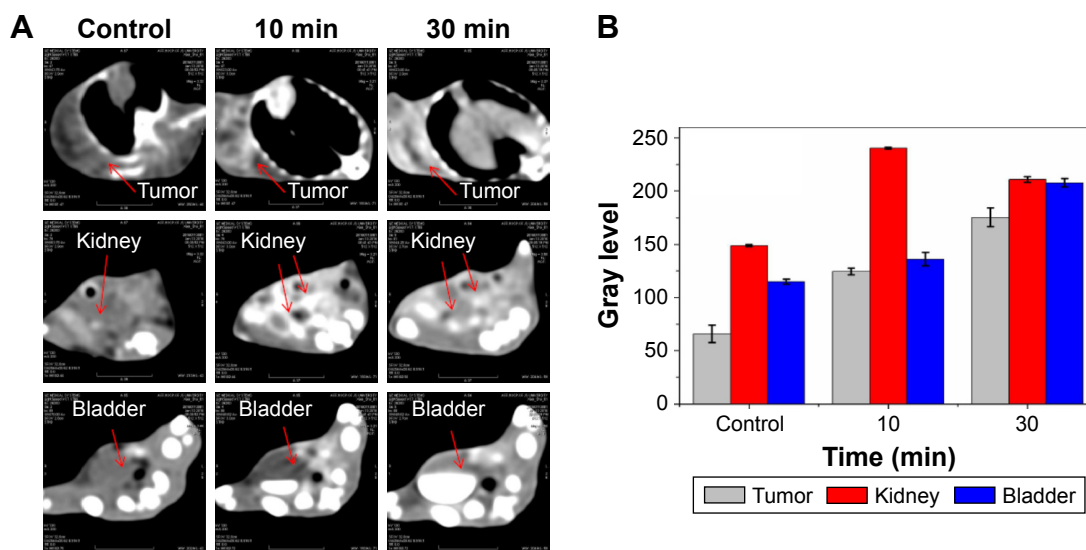


**Figure 6** (A) Herps tumor-bearing mice at preinjection and 3 h after intravenous injection of HA-Bi<sub>2</sub>O<sub>3</sub> NPs (targeted group). Arrows represent the designated areas. (B) The corresponding CT value changes in the tumor and tissue distributions of NPs *in vivo*.

**Abbreviations:** HA-Bi<sub>2</sub>O<sub>3</sub> NPs, hyaluronic acid-functionalized bismuth oxide NPs; CT, computed tomography; NPs, nanoparticles.

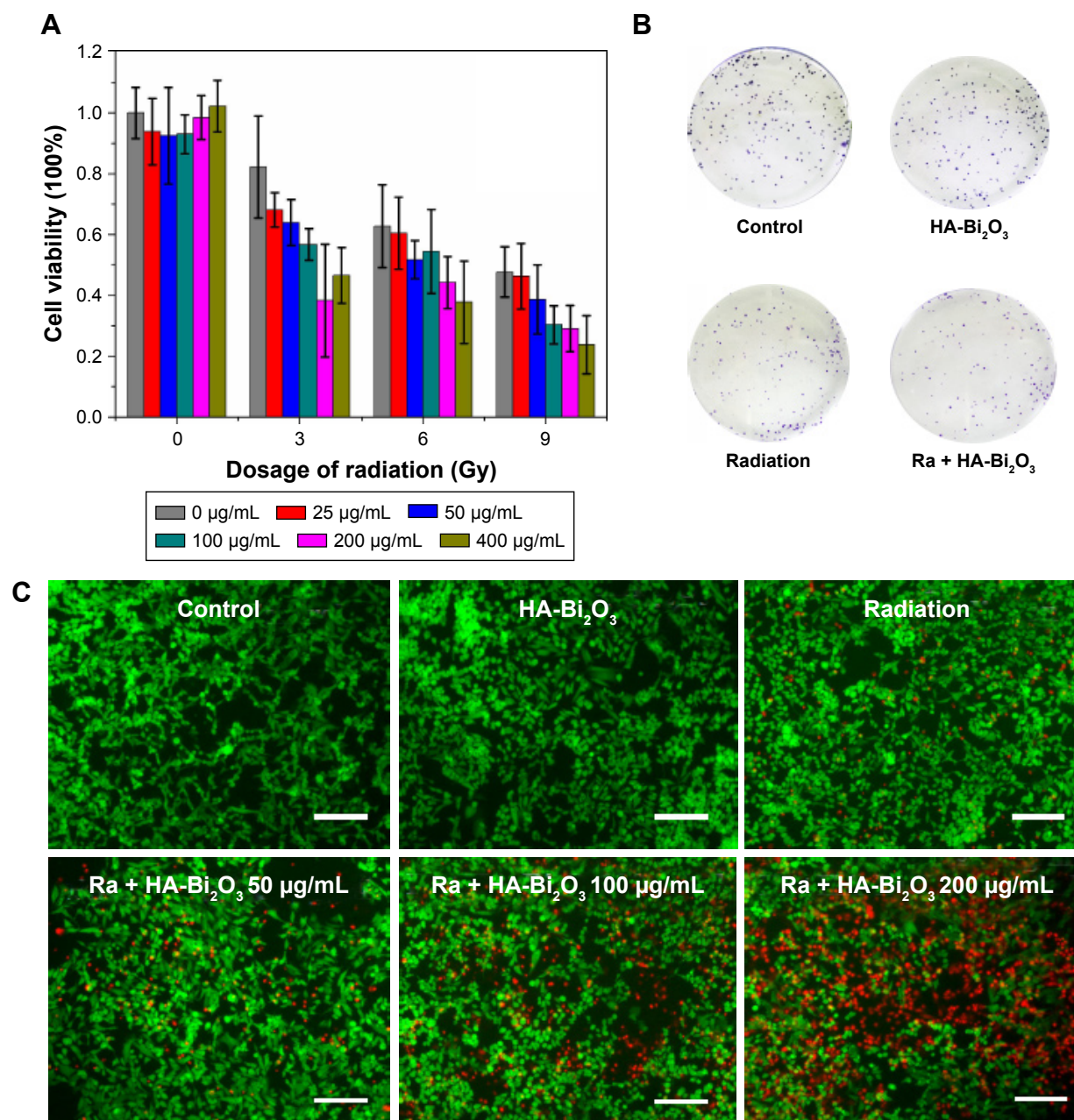


**Figure 7** (A) Combined treatment of HA-Bi<sub>2</sub>O<sub>3</sub> NPs and X-ray radiation decreased SMMC-7721 cell survival detected by clonogenic assay. SMMC-7721 cells were pretreated with HA-Bi<sub>2</sub>O<sub>3</sub> NPs at different concentrations for 24 h and then were irradiated by X-ray radiation at different dosages. (B) Colony formation of SMMC-7721 cells under the combination treatment of HA-Bi<sub>2</sub>O<sub>3</sub> NPs and radiation. (C) In vitro photo thermal effect. Live-dead staining of SMMC-7721 cells. SMMC-7721 cells were incubated with different concentrations of HA-Bi<sub>2</sub>O<sub>3</sub> NPs for 24 h and radiation. Scale bars =200 µm.

**Abbreviations:** HA-Bi<sub>2</sub>O<sub>3</sub> NPs, hyaluronic acid-functionalized bismuth oxide nanoparticles; Ra, radiation.

NPs; HA-Bi<sub>2</sub>O<sub>3</sub> NPs-only treatment had no dramatic influence on the colony-forming ability of the SMMC-7721 cells, and X-ray (6 Gy) irradiation decreased the colony-forming ability of SMMC-7721 cells to 55%. However, the treatment of HA-Bi<sub>2</sub>O<sub>3</sub> NPs with X-ray irradiation notably inhibited cell viability by 71%. The corresponding images further verified the radiosensitization of HA-Bi<sub>2</sub>O<sub>3</sub> NPs against SMMC-7721 cells (Figure 7B).

## Mechanism of radiosensitization enhancement

Flow cytometry assay and live-dead staining assay were used to further research the radiosensitization mechanism by which the combination treatment of HA-Bi<sub>2</sub>O<sub>3</sub> NPs and X-ray radiation caused cell death. As shown in Figure 7C, intensive green fluorescence without red fluorescence was observed in the SMMC-7721 cells treated with only HA-Bi<sub>2</sub>O<sub>3</sub> NPs

which verified high cell viability, but a small amount of red fluorescence was seen in the cells that received X-ray radiation treatment which indicated slight cell apoptosis. However, bright red fluorescence could be seen in the cells that received combination treatment of HA-Bi<sub>2</sub>O<sub>3</sub> NPs (200 µg/mL) and radiation (6 Gy), which demonstrated that HA-Bi<sub>2</sub>O<sub>3</sub> NPs could dramatically cause cell apoptosis. The radiosensitization mechanism of HA-Bi<sub>2</sub>O<sub>3</sub> NPs was further investigated using flow cytometry assay. Figures 8 and S7 show the flow cytometry graphs of the cells treated with HA-Bi<sub>2</sub>O<sub>3</sub> NPs with

and without radiation. Annexin-V-EGFP emission signal was plotted on the x-axis, while PI emission signal was plotted on the y-axis. The quantities of living cells, early apoptosis cells, and late apoptosis/necrosis cells were determined by the percentage of Annexin V<sup>-</sup>/PI<sup>-</sup>, Annexin V<sup>-</sup>/PI<sup>+</sup>, Annexin V<sup>+</sup>/PI<sup>-</sup>, and Annexin V<sup>+</sup>/PI<sup>+</sup>. Almost no apoptosis or necrosis of cells was observed in the group that received no radiation treatment with concentration up to 200 µg/mL. When the concentration was 100 µg/mL, after radiation, the early apoptosis rate of cells reached 30.4%, while the late apoptosis/necrosis

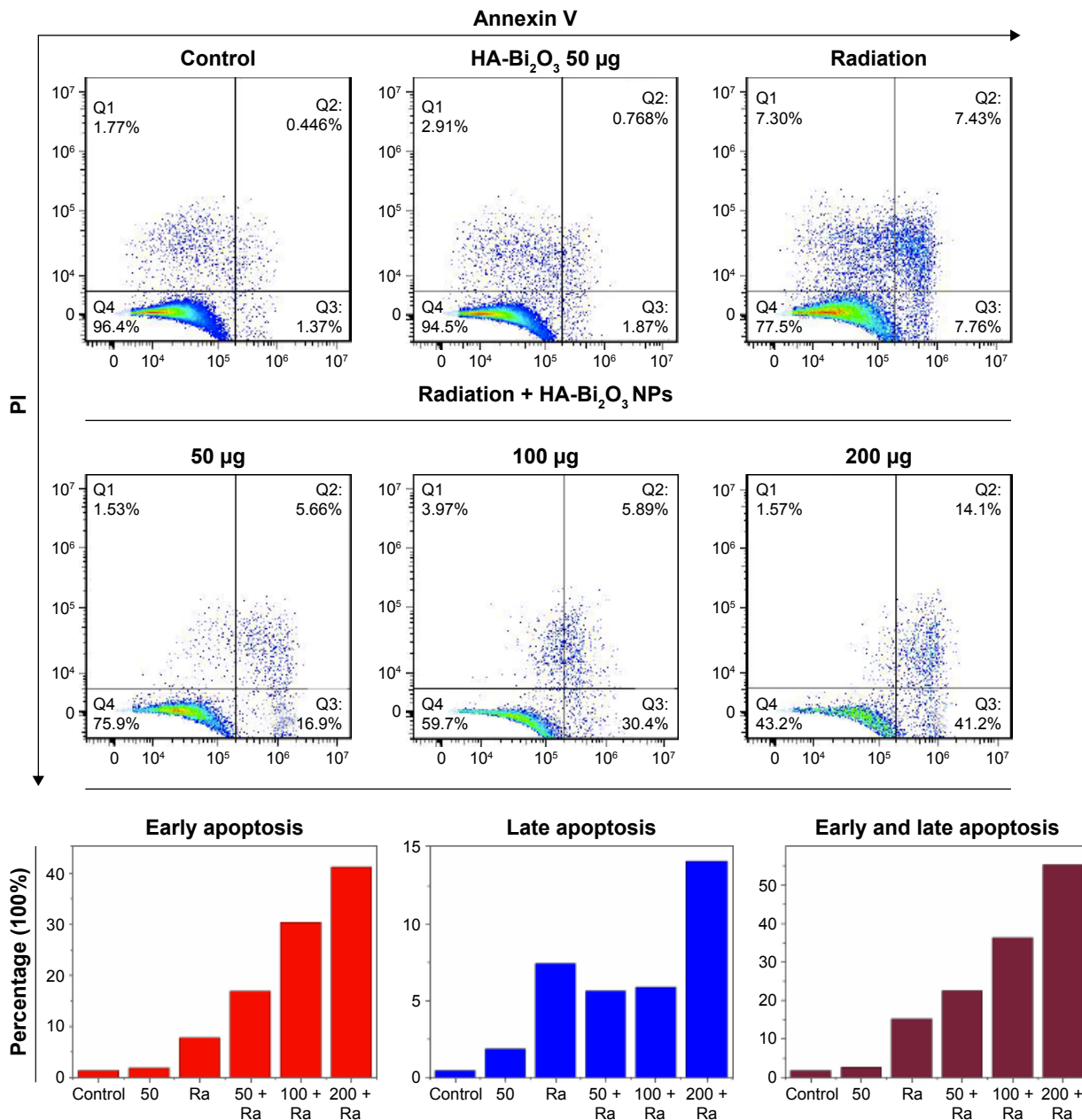


**Figure 8** Flow cytometric profiles of SMMC-7721 cells were examined to determine the percentages of early apoptosis and late apoptosis in cells with distinct treatments. Statistical data of percentage of early apoptosis and late apoptosis under different treatments are presented.

**Abbreviations:** HA-Bi<sub>2</sub>O<sub>3</sub> NPs, hyaluronic acid-functionalized bismuth oxide nanoparticles; PI, propidium iodide; Ra, radiation.

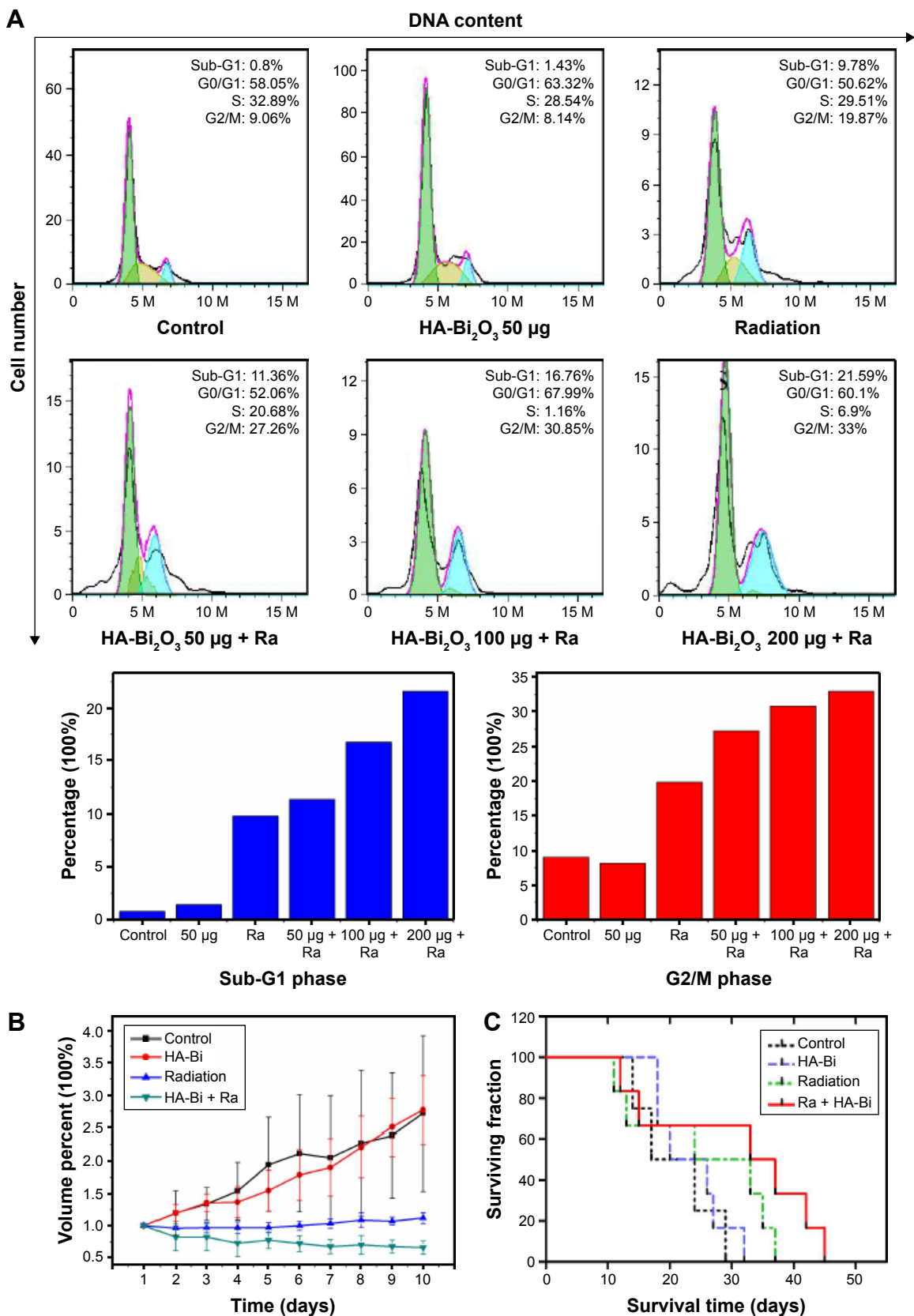


**Figure 9 (A)** Cell cycle analysis was performed using flow cytometry after treating with HA-Bi<sub>2</sub>O<sub>3</sub> NPs and irradiation. **(B)** Tumor growth inhibition profiles of the mice bearing Herps tumor treated with PBS, HA-Bi<sub>2</sub>O<sub>3</sub> NPs, and radiation at the dose of 6 Gy. **(C)** Kaplan–Meier survival analysis.

**Abbreviations:** HA-Bi<sub>2</sub>O<sub>3</sub> NPs, hyaluronic acid-functionalized bismuth oxide nanoparticles; PBS, phosphate-buffered saline; Ra, radiation.

rate was 5.89%. When the concentration was 200 µg/mL, after radiation, the early apoptosis rate of cells was 41.2%, while the late apoptosis/necrosis rate reached 14.1%. As analyzed by flow cytometry (Figures 9A and S8), radiation (6 Gy) alone slightly caused 19.87% of G2/M phase arrest, which might induce apoptosis of cells.<sup>49,50</sup> In addition, HA-Bi<sub>2</sub>O<sub>3</sub> NPs (from 0 to 200 µg/mL) activated apoptotic cell death from 0.446% to 2.34%, as reflected by the sub-G1 proportions.<sup>51</sup> However, the combination of HA-Bi<sub>2</sub>O<sub>3</sub> NPs and radiation dose-dependently increased the extent of G2/M phase arrest and cell apoptosis. For instance, combination of HA-Bi<sub>2</sub>O<sub>3</sub> NPs (200 µg/mL) and radiation at 6 Gy enhanced the proportions of G2/M phase arrest and sub-G1 peak to 33% and 21.59%, respectively, which indicated that HA-Bi<sub>2</sub>O<sub>3</sub> NPs could be an efficient alternative to improve radiosensitization enhancements for radiotherapy and have great promising applications in radiotherapy of tumors.

Generally, the combination of HA-Bi<sub>2</sub>O<sub>3</sub> NPs and X-ray irradiation exhibited a synergistic effect on the decline of cell colony formation and the cell viability in a dose-dependent manner; radiosensitization enhancement effect on the basis of flow cytometry and live–dead staining corroborated that HA-Bi<sub>2</sub>O<sub>3</sub> NPs could be an efficient alternative to improve radiosensitization enhancement for radiotherapy. The flow cytometry data revealed that cells upon X-ray irradiation treatment assisted by HA-Bi<sub>2</sub>O<sub>3</sub> NPs showed irreversible damage, and the cells could no longer function or recover from the damage.

## Radiosensitization of HA-Bi<sub>2</sub>O<sub>3</sub> NPs in vivo

To specifically examine whether the therapeutic effects of HA-Bi<sub>2</sub>O<sub>3</sub> NPs can enable overcoming the inherent radioresistance of cancer cells in vivo, ICR mice bearing 100-mm<sup>3</sup> subcutaneous Herps flank tumors were divided into four groups (n=6 per group). Notably, contrast enhancement was visible within the tumors of mice that received HA-Bi<sub>2</sub>O<sub>3</sub> NPs, which enabled CT-guided stereoscopic radiation (Figure S9). The tumor volumes of each group were measured and plotted as a function of time (Figures 9B and S10). The control group (PBS) and the group that received HA-Bi<sub>2</sub>O<sub>3</sub> NPs alone exhibited 2.5- to 3.0-fold increases in tumor volumes, respectively, compared to their original volumes, indicating that the HA-Bi<sub>2</sub>O<sub>3</sub> NPs had no influence on the tumor growth. The group that received HA-Bi<sub>2</sub>O<sub>3</sub> NPs without radiation also exhibited similar tumor growth as control group, indicating that HA-Bi<sub>2</sub>O<sub>3</sub> NPs are nontoxic without irradiation. Most

importantly, HA-Bi<sub>2</sub>O<sub>3</sub> NPs exhibited significant damage on the tumors upon radiation, which quickly gave rise to tumor necrosis 2 days postinjection and subsequent complete tumor ablation without any regrowth during 10 days postinjection, which accords with the enhanced in vitro cytotoxicity. However, the control group that received only radiation exhibited tumor regrowth 3 days postinjection, and finally increase in tumor volumes during 4–10 days postinjection. The survival time<sup>52</sup> (Figure 9C) was measured from the time of injecting ascites subcutaneously at SSD. Mice that received HA-Bi<sub>2</sub>O<sub>3</sub> NPs prior to radiation therapy exhibited a statistically significant ( $P<0.05$ ) improvement in median survival (35 days), compared to mice treated with radiation alone (24 days). Obviously, the group treated with HA-Bi<sub>2</sub>O<sub>3</sub> NPs exhibited more significant damage, which may be ascribed to their absorbing high-energy photons and emission of secondary electrons and Auger electrons. Moreover, deep penetration and uniform distribution of HA-Bi<sub>2</sub>O<sub>3</sub> NPs in tumor could also facilitate complete tumor destruction, contributing to eradication of residual cancer cells.

## Conclusion

In summary, we developed bifunctional Bi<sub>2</sub>O<sub>3</sub> NPs for effective CT imaging and radiosensitization of tumor by HA functionalization. On coating with HA, the as-prepared HA-Bi<sub>2</sub>O<sub>3</sub> NPs enabled realizing the feasibility of specific targeting to cancer cells overexpressing CD44 receptors. The HA-Bi<sub>2</sub>O<sub>3</sub> NPs revealed favorable solubility in water and excellent biocompatibility confirming its series of biological and chemical effects. Furthermore, the heavy metal-based HA-Bi<sub>2</sub>O<sub>3</sub> NPs could be effectively excreted throughout the renal clearance, reflecting low toxicity. The resultant HA-Bi<sub>2</sub>O<sub>3</sub> NPs encapsulated with Bi atoms not only excellently overcame the inherent radioresistance of cancer cells by absorbing the high-energy photons and emitting secondary electrons and Auger electrons but also possessed high X-ray attenuation coefficient in favor of CT imaging-guided radiotherapy with a significant radiosensitization enhancement. Thus, the novel HA-Bi<sub>2</sub>O<sub>3</sub> NPs have great promising applications in diagnosis and radiotherapy of tumors.

## Acknowledgments

This research was supported by the National Natural Science Foundation of China (81301316 and 31200676), China Postdoctoral Science Foundation (2013M540425, 2014T70487 and 2015M571705), Health and Family Planning Commission of Jiangsu Province scientific research subject

(H201557), Natural Science Foundation of Jiangsu Province (BK20161317), and Senior Talents Scientific Research Foundation of Jiangsu University (13JDG022 and 11JDG113).

## Disclosure

The authors report no conflicts of interest in this work.

## References

- Huang Y, Luo Y, Zheng W, Chen T. Rational design of cancer-targeted BSA protein nanoparticles as radiosensitizer to overcome cancer radioresistance. *ACS Appl Mater Interfaces*. 2014;6(21):19217–19228.
- Lord CJ, Ashworth A. The DNA damage response and cancer therapy. *Nature*. 2012;481(7381):287–294.
- Fan W, Shen B, Bu W, et al. Rattle-structured multifunctional nanotheranostics for synergetic chemo-/radiotherapy and simultaneous magnetic/luminescent dual-mode imaging. *J Am Chem Soc*. 2013;135(17):6494–6503.
- Pan Y, Zhang Q, Atsaves V, Yang H, Claret FX. Suppression of Jab1/CSN5 induces radio- and chemo-sensitivity in nasopharyngeal carcinoma through changes to the DNA damage and repair pathways. *Oncogene*. 2013;32(22):2756–2766.
- Xing H, Zheng X, Ren Q, et al. Computed tomography imaging-guided radiotherapy by targeting upconversion nanocubes with significant imaging and radiosensitization enhancements. *Sci Rep*. 2013;3:1751.
- Liu Y, Zhang N. Gadolinium loaded nanoparticles in theranostic magnetic resonance imaging. *Biomaterials*. 2012;33(21):5363–5375.
- Luo Z, Ding X, Hu Y, et al. Engineering a hollow nanocontainer platform with multifunctional molecular machines for tumor-targeted therapy *in vitro* and *in vivo*. *ACS Nano*. 2013;7(11):10271–10284.
- Kakuta T, Takashima Y, Nakahata M, Otsubo M, Yamaguchi H, Harada A. Preorganized hydrogel: self-healing properties of supramolecular hydrogels formed by polymerization of host-guest-monomers that contain cyclodextrins and hydrophobic guest groups. *Adv Mater*. 2013;25(20):2849–2853.
- Peng L, Peng X, Liu B, Wu C, Xie Y, Yu G. Ultrathin two-dimensional MnO<sub>2</sub>/graphene hybrid nanostructures for high-performance, flexible planar supercapacitors. *Nano Lett*. 2013;13(5):2151–2157.
- Caracciolo G, Cardarelli F, Pozzi D, et al. Selective targeting capability acquired with a protein corona adsorbed on the surface of 1,2-dioleoyl-3-trimethylammonium propane/DNA nanoparticles. *ACS Appl Mater Interfaces*. 2013;5(24):13171–13179.
- Taratula O, Kuzmov A, Shah M, Garbuzenko OB, Minko T. Nanostructured lipid carriers as multifunctional nanomedicine platform for pulmonary co-delivery of anticancer drugs and siRNA. *J Control Release*. 2013;171(3):349–357.
- Park S, Kang S, Chen X, et al. Tumor suppression via paclitaxel-loaded drug carriers that target inflammation marker upregulated in tumor vasculature and macrophages. *Biomaterials*. 2013;34(2):598–605.
- Shilo M, Reuveni T, Motiei M, Popovtzer R. Nanoparticles as computed tomography contrast agents: current status and future perspectives. *Nanomedicine (Lond)*. 2012;7(2):257–269.
- Luchette M, Korideck H, Makrigiorgos M, Tillement O, Berbeco R. Radiation dose enhancement of gadolinium-based AGuIX nanoparticles on HeLa cells. *Nanomedicine*. 2014;10(8):1751–1755.
- Le DG, Miladi I, Alric C, et al. Toward an image-guided microbeam radiation therapy using gadolinium-based nanoparticles. *ACS Nano*. 2011;5(12):9566–9574.
- Dufort S, Bianchi A, Henry M, et al. Nebulized gadolinium-based nanoparticles: a theranostic approach for lung tumor imaging and radiosensitization. *Small*. 2015;11(2):215–221.
- Xing H, Bu W, Zhang S, et al. Multifunctional nanoprobe for upconversion fluorescence, MR and CT trimodal imaging. *Biomaterials*. 2012;33(4):1079–1089.
- Ma M, Huang Y, Chen H, et al. Bi<sub>2</sub>S<sub>3</sub>-embedded mesoporous silica nanoparticles for efficient drug delivery and interstitial radiotherapy sensitization. *Biomaterials*. 2015;37:447–455.
- Zhang M, Ju H, Zhang L, et al. Engineering iodine-doped carbon dots as dual-modal probes for fluorescence and X-ray CT imaging. *Int J Nanomedicine*. 2015;10:6943–6953.
- Chen J, Yang XQ, Qin MY, Zhang XS, Xuan Y, Zhao YD. Hybrid nanoprobe of bismuth sulfide nanoparticles and CdSe/ZnS quantum dots for mouse computed tomography/fluorescence dual mode imaging. *J Nanobiotechnology*. 2015;13:76.
- Chen J, Yang XQ, Meng YZ, et al. *In vitro* and *in vivo* CT imaging using bismuth sulfide modified with a highly biocompatible Pluronic F127. *Nanotechnology*. 2014;25(29):295103.
- Rivera EJ, Tran LA, Hernández-Rivera M, et al. Bismuth@US-tubes as a potential contrast agent for X-ray imaging applications. *J Mater Chem B Mater Biol Med*. 2013;1(37):10.1039/C3TB20742K.
- Li Z, Hu Y, Howard KA, et al. Multifunctional bismuth selenide nanocomposites for antitumor thermo-chemotherapy and imaging. *ACS Nano*. 2016;10(1):984–997.
- Grigas J, Talik E, Lazauskas V. X-ray photoelectron spectra and electronic structure of Bi<sub>2</sub>S<sub>3</sub> crystals. *Phys Status Solidi*. 2002;232(2):220–230.
- Thomson JW, Lawson G, O'Brien P, et al. Flash nano-welding: investigation and control of the photothermal response of ultrathin bismuth sulfide nanowire films. *Adv Mater*. 2010;22(39):4395–4400.
- Martinez L, Bernechea M, de Arquer F, Konstantatos G. Near IR-sensitive, non-toxic polymer/nanocrystal solar cells employing Bi<sub>2</sub>S<sub>3</sub> as the electron acceptor. *Adv Energy Mater*. 2011;1(6):1029–1035.
- Malakooti R, Cademartiri L, Akçakir Y, Petrov S, Migliori A, Ozin GA. Shape-controlled Bi<sub>2</sub>S<sub>3</sub> nanocrystals and their plasma polymerization into flexible films. *Adv Mater*. 2006;18(16):2189–2194.
- Sigman MB, Korgel BA. Solventless synthesis of Bi<sub>2</sub>S<sub>3</sub> (bismuthinite) nanorods, nanowires, and nanofabric. *Chem Mater*. 2005;17(7):1655–1660.
- Yao MH, Ma M, Chen Y, et al. Multifunctional Bi<sub>2</sub>S<sub>3</sub>/PLGA nanocapsule for combined HIFU/radiation therapy. *Biomaterials*. 2014;35(28):8197–8205.
- Alqathami M, Blencowe A, Yeo UJ, et al. Enhancement of radiation effects by bismuth oxide nanoparticles for kilovoltage x-ray beams: a dosimetric study using a novel multi-compartment 3D radiochromic dosimeter. *J Phys*. 2013;44(1):012025.
- Preihs C, Arambula JF, Lynch VM, Siddik ZH, Sessler JL. Bismuth- and lead-texaphyrin complexes: towards potential  $\alpha$ -core emitters for radiotherapy. *Chem Commun (Camb)*. 2010;46(42):7900–7902.
- Goh EJ, Kim KS, Kim YR, et al. Bioimaging of hyaluronic acid derivatives using nanosized carbon dots. *Biomacromolecules*. 2012;13(8):2554–2561.
- Lee MY, Yang JA, Jung HS, et al. Hyaluronic acid-gold nanoparticle/interferon  $\alpha$  complex for targeted treatment of hepatitis C virus infection. *ACS Nano*. 2012;6(11):9522–9531.
- Abdullah-Al-Nahain, Lee JE, In I, et al. Target delivery and cell imaging using hyaluronic acid-functionalized graphene quantum dots. *Mol Pharm*. 2013;10(10):3736–3744.
- Petoral Jr RM, Söderlind F, Klasson A, et al. Synthesis and characterization of Tb<sup>3+</sup>-doped Gd<sub>2</sub>O<sub>3</sub> nanocrystals: a bifunctional material with combined fluorescent labeling and MRI contrast agent properties. *J Phys Chem*. 2009;113(17):6913–6920.
- Zhang M, Zhao X, Fang Z, et al. Fabrication of HA/PEI-functionalized carbon dots for tumor targeting, intracellular imaging and gene delivery. *RSC Adv*. 2017;7(6):3369–3375.
- Zhang M, Fang Z, Zhao X, et al. Hyaluronic acid functionalized nitrogen-doped carbon quantum dots for targeted specific bioimaging. *RSC Adv*. 2016;6(107):104979–104984.
- Du F, Yuan J, Zhang M, et al. Facile synthesis of biocompatible nitrogen-doped carbon dots for bioimaging. *RSC Adv*. 2014;4(71):37536–37541.



39. Li J, Zheng L, Cai H, et al. Polyethyleneimine-mediated synthesis of folic acid-targeted iron oxide nanoparticles for *in vivo* tumor MR imaging. *Biomaterials*. 2013;34(33):8382–8392.
40. Du F, Zhang L, Zhang L, et al. Engineered gadolinium-doped carbon dots for magnetic resonance imaging-guided radiotherapy of tumors. *Biomaterials*. 2017;121:109–120.
41. Huang Y, Wang W, Zhang Q, et al. In situ fabrication of  $\alpha$ -Bi<sub>2</sub>O<sub>3</sub>/(BiO)<sub>2</sub>CO<sub>3</sub> nanoplate heterojunctions with tunable optical property and photocatalytic activity. *Sci Rep*. 2016;6:23435.
42. Wang Y, Yang T, Ke H, et al. Smart albumin-biomineralized nanocomposites for multimodal imaging and photothermal tumor ablation. *Adv Mater*. 2015;27(26):3874–3882.
43. Du F, Li J, Hua Y, et al. Multicolor nitrogen-doped carbon dots for live cell imaging. *J Biomed Nanotechnol*. 2015;11(5):780–788.
44. Nami B, Donmez H, Koçak N. Autophagy reduces subpopulation of CD44<sup>+</sup>/CD24<sup>+</sup>/low phenotype cancer stem cells in MCF7 and Hep-2 cells culture. *Stem Cell Res*. 2015;(3):e1002.
45. Yu GF, Chen YM, Yan YH, Zeng WT, Zhu KL. Effect of arsenic trioxide on invasion and metastasis of human hepatocarcinoma cells SMMC-7721 *in vitro*. *J Mod Oncol*. 2011;7(19):1282–1284.
46. Wang J, Chen H, Ji H, Zhang ZG. Effect of earthworm fibrinolytic enzyme on growth of xenografted tumor of hepatocellular carcinoma (HCC) and expression of CD44v6. *Cancer Res Prev Treat*. 2009;36(5):375–379.
47. Al Zaki A, Joh D, Cheng Z, et al. Gold-loaded polymeric micelles for computed tomography-guided radiation therapy treatment and radiosensitization. *ACS Nano*. 2014;8(1):104–112.
48. Dong K, Ju E, Liu J, Han X, Ren J, Qu X. Ultrasmall biomolecule-anchored hybrid GdVO<sub>4</sub> nanophosphors as a metabolizable multimodal bioimaging contrast agent. *Nanoscale*. 2014;6(20):12042–12049.
49. Campisi J, d'Adda di Fagnana F. Cellular senescence: when bad things happen to good cells. *Nat Rev Mol Cell Biol*. 2007;8(9):729–740.
50. Rao PC, Begum S, Sahai M, Sriram DS. Coptisine-induced cell cycle arrest at G2/M phase and reactive oxygen species-dependent mitochondria-mediated apoptosis in non-small-cell lung cancer A549 cells. *Tumour Biol*. 2017;39(3):1010428317694565.
51. Liu DX, Greene LA. Neuronal apoptosis at the G1/S cell cycle checkpoint. *Cell Tissue Res*. 2001;305(2):217–228.
52. Liu J, Guo B, Chen Z, et al. miR-125b promotes MLL-AF9-driven murine acute myeloid leukemia involving a VEGFA-mediated non-cell-intrinsic mechanism. *Blood*. 2017;129(11):1491–1502.

### Supplementary materials

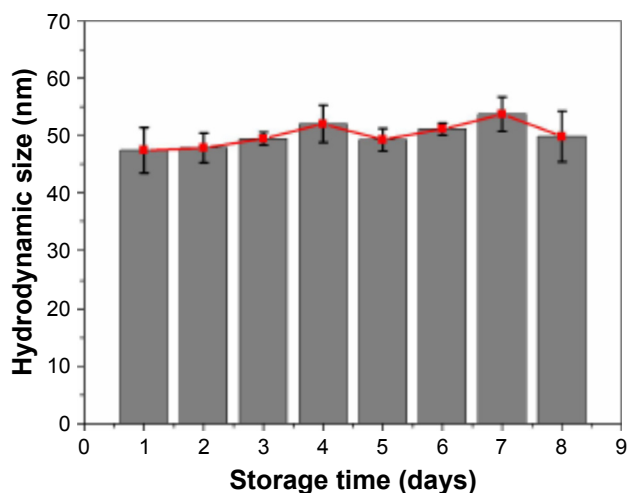


**Figure S1** Hydrodynamic diameter of HA-Bi<sub>2</sub>O<sub>3</sub> NPs in 90% PBS with 10% FBS during 8 days of storage.

**Abbreviations:** HA-Bi<sub>2</sub>O<sub>3</sub> NPs, hyaluronic acid-functionalized bismuth oxide nanoparticles; PBS, phosphate-buffered saline.

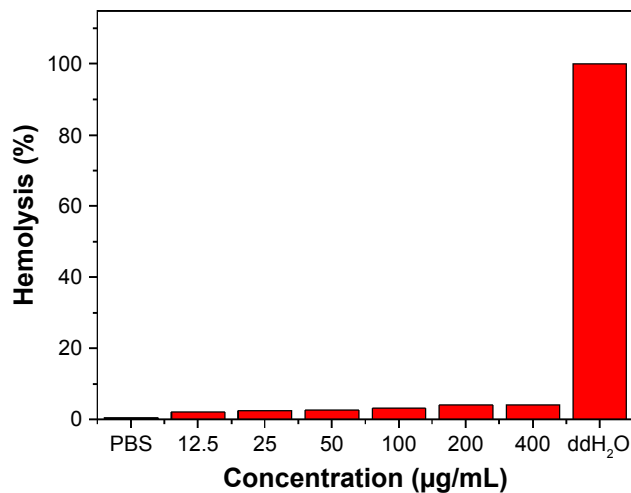


**Figure S4** Concentration–hemolysis relation in hemolysis assay.

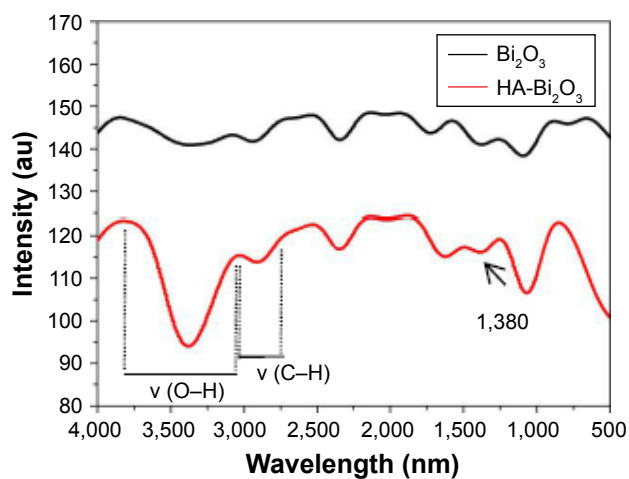


**Figure S2** FT-IR spectrum of HA-Bi<sub>2</sub>O<sub>3</sub> NPs and naked Bi<sub>2</sub>O<sub>3</sub> NPs.

**Abbreviations:** FT-IR, Fourier transform infrared; HA-Bi<sub>2</sub>O<sub>3</sub> NPs, hyaluronic acid-functionalized Bi<sub>2</sub>O<sub>3</sub> NPs; Bi<sub>2</sub>O<sub>3</sub> NPs, bismuth oxide nanoparticles.

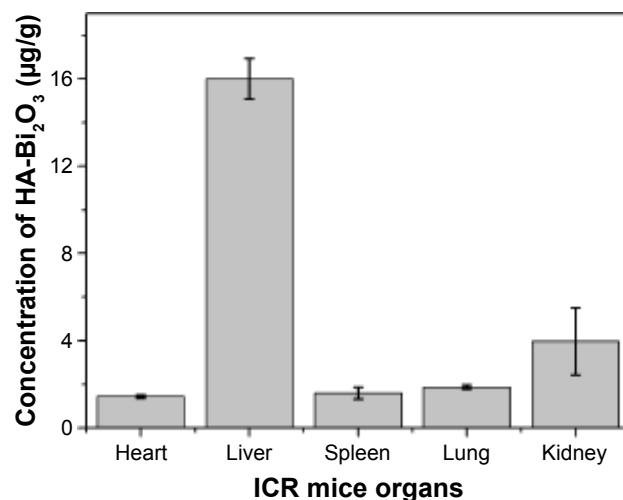


**Figure S5** Distribution of Bi element from various normal tissues at 24 h post-injection of HA-Bi<sub>2</sub>O<sub>3</sub> NPs at the dose of 40 mg/kg.

**Abbreviation:** HA-Bi<sub>2</sub>O<sub>3</sub> NPs, hyaluronic acid-functionalized bismuth oxide nanoparticles.

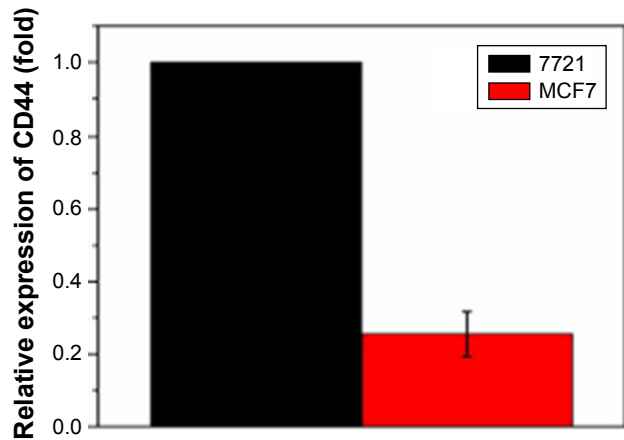


**Figure S3** CD44 expression determined by real-time PCR in distinct cancer cells.

**Abbreviation:** PCR, polymerase chain reaction.



**Figure S6** In vivo three-dimensional volume rendering and transverse slice CT images.

**Note:** Circles represent the designated area.

**Abbreviation:** CT, computed tomography.

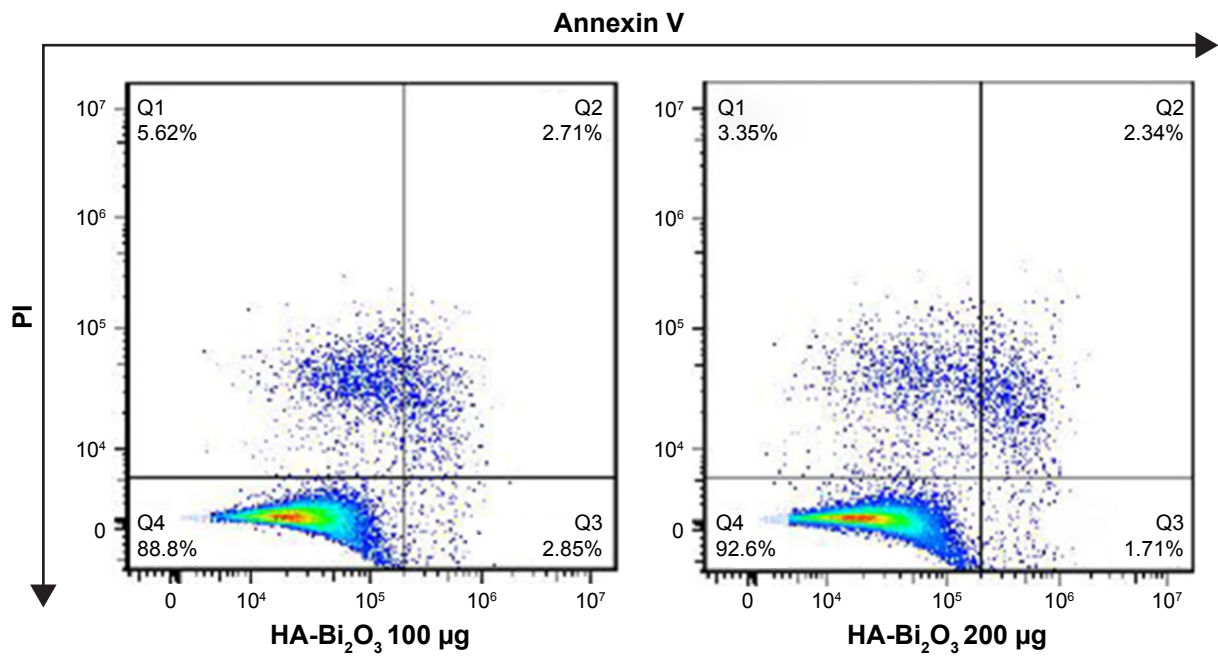


**Figure S7** Flow cytometric profiles of SMMC-7721 cells were examined to determine the percentages of early apoptosis and late apoptosis cells with different concentrations of HA-Bi<sub>2</sub>O<sub>3</sub> NPs.

**Abbreviations:** HA-Bi<sub>2</sub>O<sub>3</sub> NPs, hyaluronic acid-functionalized bismuth oxide nanoparticles; PI, propidium iodide.

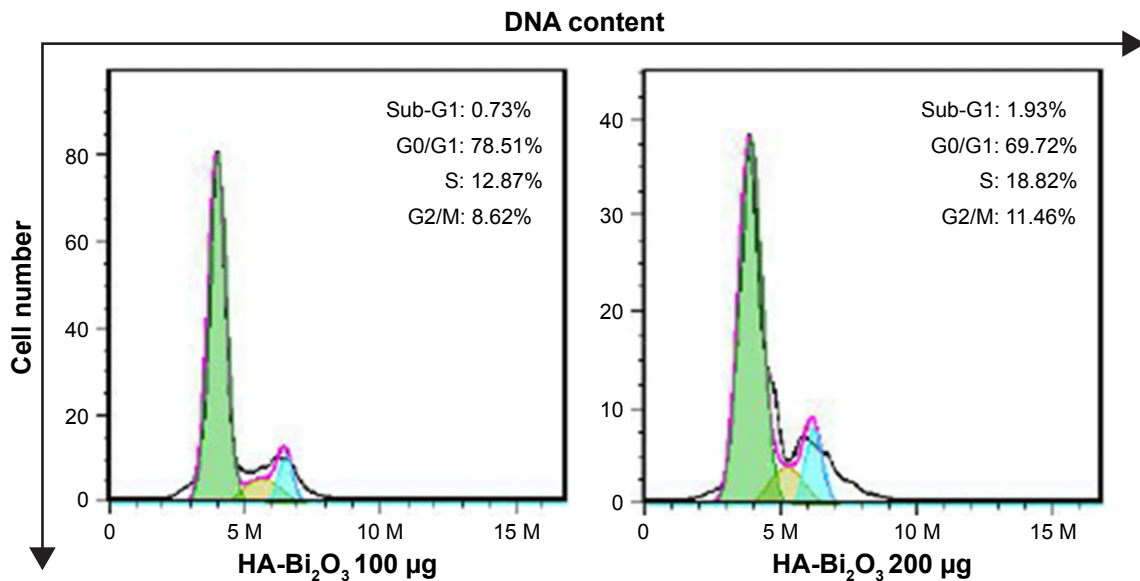


**Figure S8** Flow cytometric profiles of SMMC-7721 cells were examined to determine the G2/M phase arrest and apoptosis with different concentrations of HA-Bi<sub>2</sub>O<sub>3</sub> NPs.

**Abbreviation:** HA-Bi<sub>2</sub>O<sub>3</sub> NPs, hyaluronic acid-functionalized bismuth oxide nanoparticles.

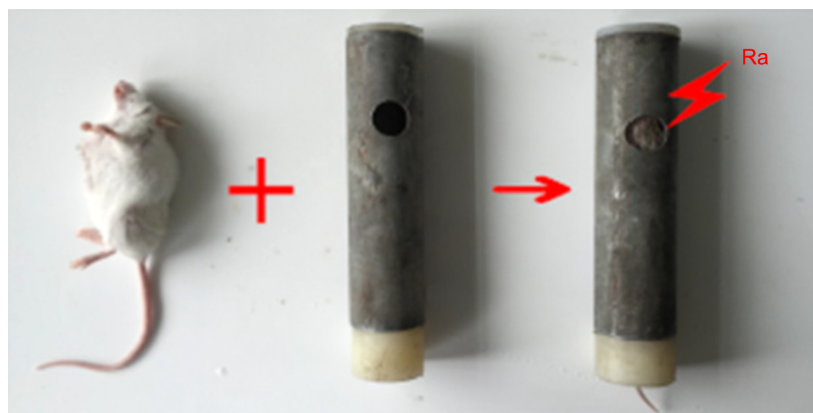


**Figure S9** Self-prepared device for mice radiotherapy.

**Note:** The mice were placed in a leaden device which exposed parts of the subcutaneous tumor to radiation treatment.

**Abbreviation:** Ra, radiation.

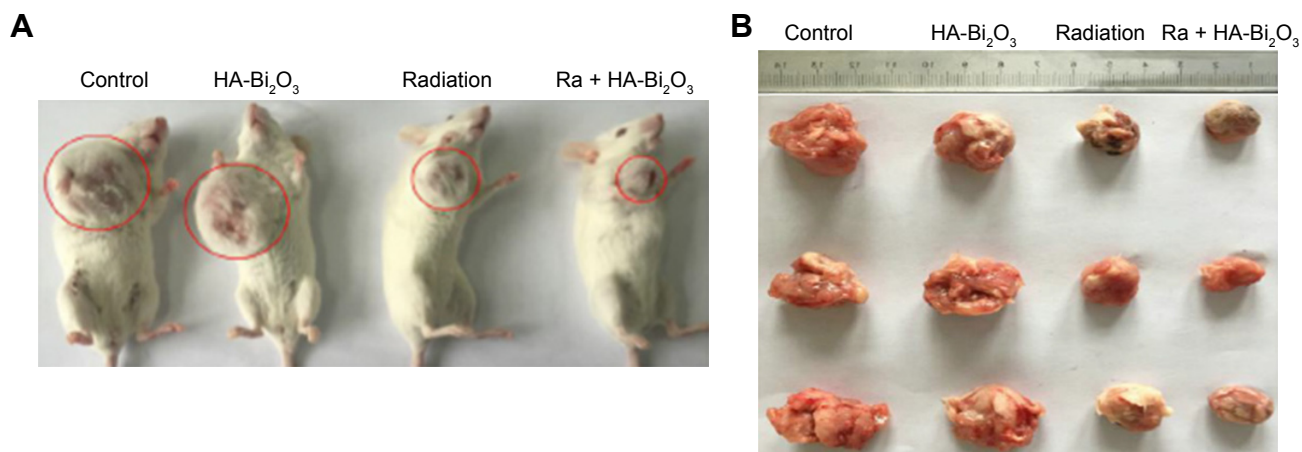


**Figure S10** Photographs of the tumors extracted from the mice bearing Herps tumor at the end of the radiation experiment.

**Notes:** (A) Scope of subcutaneous tumors (red circles). (B) The subcutaneous tumors were recovered from the mice with three replications.

**Abbreviations:** HA-Bi<sub>2</sub>O<sub>3</sub> NPs, hyaluronic acid-functionalized bismuth oxide nanoparticles; Ra, radiation.

International Journal of Nanomedicine

Publish your work in this journal

The International Journal of Nanomedicine is an international, peer-reviewed journal focusing on the application of nanotechnology in diagnostics, therapeutics, and drug delivery systems throughout the biomedical field. This journal is indexed on PubMed Central, MedLine, CAS, SciSearch®, Current Contents®/Clinical Medicine,

Submit your manuscript here: <http://www.dovepress.com/international-journal-of-nanomedicine-journal>

Dovepress

Journal Citation Reports/Science Edition, EMBASE, Scopus and the Elsevier Bibliographic databases. The manuscript management system is completely online and includes a very quick and fair peer-review system, which is all easy to use. Visit <http://www.dovepress.com/testimonials.php> to read real quotes from published authors.